

# Quantum–Classical Separation in Bounded-Resource Tasks Arising from Measurement Contextuality

Google Quantum AI<sup>†</sup>

The prevailing view is that quantum phenomena can be harnessed to tackle certain problems beyond the reach of classical approaches. Quantifying this capability as a quantum–classical separation and demonstrating it on current quantum processors has remained elusive. Using a superconducting qubit processor, we show that quantum contextuality enables certain tasks to be performed with success probabilities beyond classical limits. With a few qubits, we illustrate quantum contextuality with the magic square game, as well as quantify it through a Kochen–Specker–Bell inequality violation. To examine many-body contextuality, we implement the N-player GHZ game and separately solve a 2D hidden linear function problem, exceeding classical success rate in both. Our work proposes novel ways to benchmark quantum processors using contextuality-based algorithms.

It is widely believed that distinct non-classical features allow certain quantum algorithms to outperform their classical counterparts, an expectation that has motivated extensive research on quantum processors. Yet proving separations between computational algorithms is extremely challenging; to date, no unconditional proof of quantum advantage exists for a general computational model. Nevertheless, a few rare algorithms demonstrate provable separation, and hence advantages, under specific bounded resources beyond metered memory and time. On the hardware side, however, there is still no direct experimental measurement of the quantum–classical separation for these algorithms, nor of the degree of ‘quantumness’ in the corresponding many-body states, as sufficiently large quantum processors have only recently become available.

Beyond quantum–classical separations, a central question is which unique aspect of quantum phenomena constitutes a computational resource. While entanglement is well understood as a resource for quantum communication, some studies suggest that contextuality could be the key resource enabling the superiority of quantum computation [1–8]. The role of contextuality in many-body computation, unlike in few-body tasks, remains poorly understood. Most studies on the information-theoretic aspects of many-body quantum states have focused on other aspects, entanglement for example, with only a few exceptions examining their contextuality [3, 9–14]. Although central to modern views on quantum mechanics, contextuality has seen few experimental studies [15–28].

Quantum measurement contextuality arises from the observation that in certain quantum systems the outcomes of observables depend on the measurement context and are not predetermined [29, 30]. The discussion of this phenomenon traces back to the famous EPR argument and Einstein’s question, “*Is the moon there when nobody looks?*” [31, 32], reflecting the realist belief that physical properties exist objectively and independently of observation. This notion of pre-existing properties became central to the EPR (Einstein–Podolsky–Rosen) argument for the incompleteness of quantum theory [33], a view that was ultimately challenged by experimental tests [34, 35].

A set of measurements on a tripartite quantum state  $\Psi = (|000\rangle - |111\rangle)/\sqrt{2}$  can illustrate the impossibility of assigning pre-defined values to physical observables [36, 37]. When measuring the 3-qubit Pauli oper-

ators  $A = X_1Y_2Y_3$ ,  $B = Y_1X_2Y_3$ , and  $C = Y_1Y_2X_3$ , the outcomes are always  $+1$ . One can measure  $A$ , for example, by simultaneously measuring  $X_1$ ,  $Y_2$ , and  $Y_3$ , obtaining outcomes  $x_1$ ,  $y_2$ , and  $y_3$ , respectively, which are each  $\pm 1$ , such that product  $x_1y_2y_3$  is always  $+1$ . However, a measurement of  $D = X_1X_2X_3$ , yields  $-1$  even though multiplying  $x_1y_2y_3 = +1$ ,  $y_1x_2y_3 = +1$ , and  $y_1y_2x_3 = +1$  would give  $x_1x_2x_3 = +1$ , which one would expect to agree with the measurement of  $D$  if one assumed that all of the  $x_i$  and  $y_i$  had pre-determined values. This counterintuitive finding highlights the subtle role of measurement context in describing what is observed in quantum systems.

Quantum contextuality-based tasks exploit classically-impossible correlations to design games where players can succeed despite being unable to communicate [38, 39]. In these so-called quantum pseudo-telepathy games, players achieve higher winning probabilities by sharing an entangled quantum state and conditioning their strategies on measurement outcomes, compared to using a classical set of pre-agreed instructions. To experimentally illustrate contextuality, we implement the magic square game [40–44] on our superconducting qubit processor. This is a cooperative game featuring two players, Alice and Bob, and a referee. The rules of the game are as follows.

- i. *Resource sharing*: Initially, players are allowed to communicate and share a strategy.
- ii. *Imposing non-communication*: Alice and Bob are separated, and the referee randomly assigns to Alice  $j$ -th row and to Bob  $k$ -th column of a  $3 \times 3$  table that they must fill with  $a_{j,k} \in \{\pm 1\}$ .
- iii. *Constraint*: The products of the numbers for Alice’s assigned row must be  $+1$ , and for Bob’s column must be  $-1$ ,

$$R_j = \prod_k a_{j,k} = +1, \quad C_k = \prod_j a_{j,k} = -1. \quad (1)$$

- iv. *Winning condition*: They win if they have the same number at the intersecting cell.

Any classical strategy that they could share before they know their row and column assignment can be represented as a  $3 \times 3$  table of the values  $\pm 1$ . In this table, the number

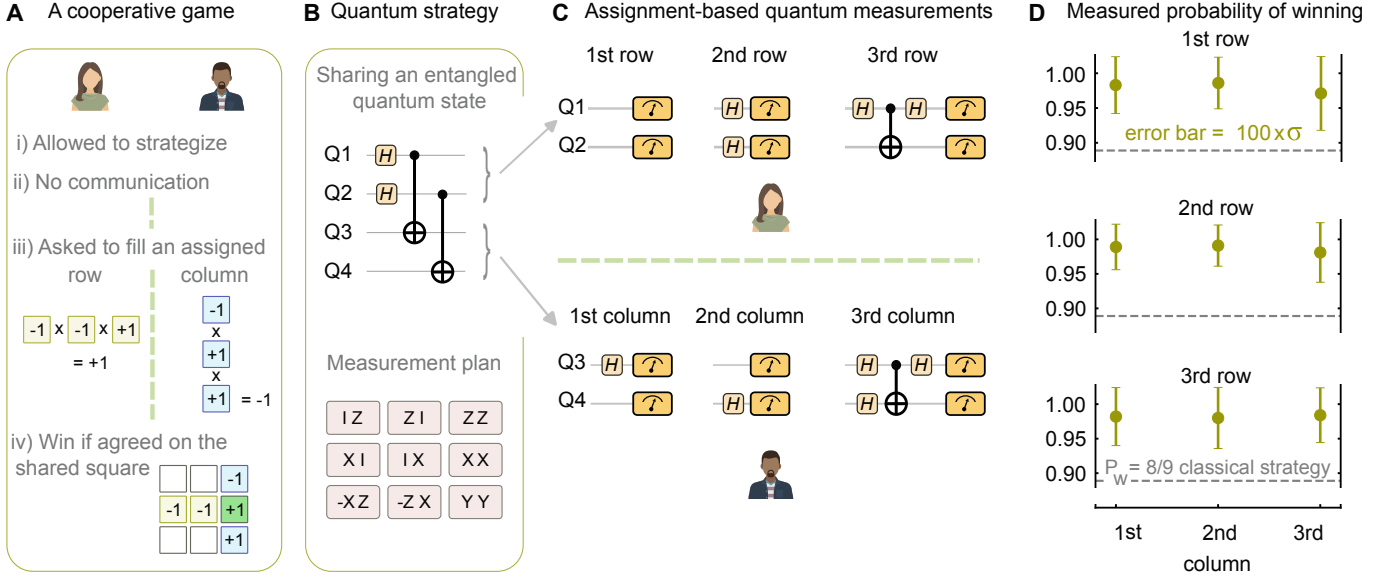


FIG. 1. **The Mermin-Peres magic square game.** (A) The rules of this game. The green dashed line indicates the incommunicado constraint. Alice gets a row and Bob a column of a  $3 \times 3$  table; entries must satisfy row products  $= +1$ , column products  $= -1$ , and they win if their shared cell matches. (B) Leveraging a quantum strategy, the players share two Bell pairs and agree on what measurements to perform for each assigned row (Alice) or column (Bob), using the measurement plan table, where first Pauli in each cell refers to their first qubit. (C) Each player performs two simultaneous measurements and, given the product constraint rule (iii), they infer the third value needed to fill out their assigned row or column. (D) Measured probability of winning the game when played on our processor, shown for 9 distinct games (row or column assignment) sorted by where the assigned rows and columns intersect. The average probability of winning is  $P_w = 0.9830 \pm 0.0001$ . Each game is played  $N_s = 100,000$  times and the error bar plotted for each game is 100 times the statistical uncertainty derived from the binomial distribution.

$-1$  would need to appear an even number of times for each row and an odd number of times for each column. Therefore, the total number of  $-1$  needs to be even and odd at the same time, which is impossible. Thus there is no classical strategy that wins every time. It can be seen that the best classical strategy results in a winning probability of  $8/9$ , under the assumption that the referee assigns them rows and columns uniformly at random. Here, we implement a quantum pseudo-telepathy strategy that enables players to win the game with probability  $P_w = 1$ . Starting with a pair of Bell pairs,

$$|\Psi\rangle = \left(\frac{|00\rangle + |11\rangle}{\sqrt{2}}\right)_{Q1,Q3} \otimes \left(\frac{|00\rangle + |11\rangle}{\sqrt{2}}\right)_{Q2,Q4}, \quad (2)$$

Alice and Bob each take half of each Bell pair, i.e. Alice takes  $Q1$  and  $Q2$ , and Bob takes  $Q3$  and  $Q4$ . After they are separated and informed about their row and column assignment, they each use the pre-agreed Table I to select which measurements they should make. To play the game, we use a  $2 \times 2$  square of qubits. We prepare Bell pairs between the vertical pairs and then identify the top two qubits as Alice and the bottom two as Bob.

In Fig. 1(D) we show the result of playing the 9 games, sorted based on the intersection of the assigned row and column. Each of these distinct games is played  $N_s = 100,000$  times, yielding an average winning probability of  $P_w = 0.9830 \pm 0.0001$ . The uncertainty in each of the nine distinct games comes from a binomial distribution and is proportional to  $1/\sqrt{N_s}$ , and can be made much smaller

|       | column 1   | column 2   | column 3  |
|-------|------------|------------|-----------|
| row 1 | $I_1 Z_2$  | $Z_1 I_2$  | $Z_1 Z_2$ |
| row 2 | $X_1 I_2$  | $I_1 X_2$  | $X_1 X_2$ |
| row 3 | $-X_1 Z_2$ | $-Z_1 X_2$ | $Y_1 Y_2$ |

TABLE I. The Mermin-Peres table is a set of measurement instructions that the two players can use to deterministically win the game,  $P_w = 1$ , if given noiseless quantum resources.

by increasing  $N_s$ . The higher  $P_w$  than classical bound values are rooted in the non-commutativity of quantum observables. These scores illustrate why quantum theory requires matrix representations, unlike classical physics with scalar observables. The threshold where quantum advantage disappears marks the point beyond which matrix mechanics is no longer needed.

To quantify the degree of contextuality for our processors we use an inequality, analogous to the Bell inequality. The Bell-Kochen-Specker (BKS) theorem states that no non-contextual hidden-variables (NCHV) theory can reproduce the predictions of quantum mechanics for correlations between measurement outcomes of some sets of observables [45–48]. Cabello [49] and others [50] derive a set of inequalities that are satisfied by any NCHV theory but are violated by quantum mechanics for *any* quantum state. These inequalities bound certain linear combinations of ensemble averages of correlations between measurement outcomes of compatible observables; thus creating a separation between the predicted outcomes of quan-

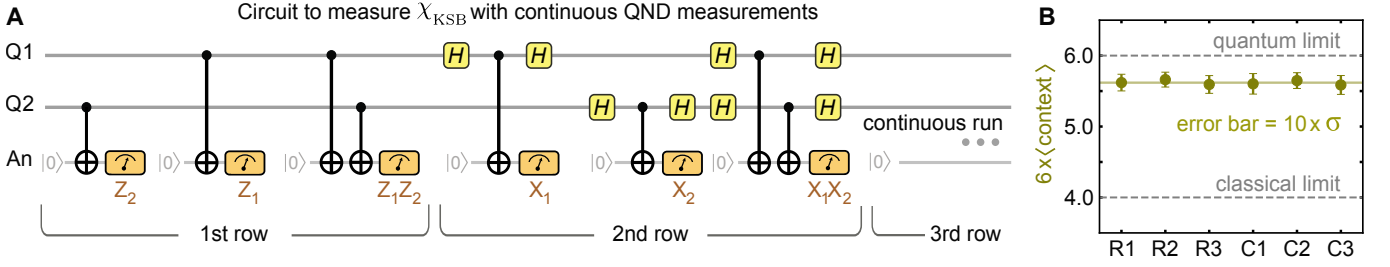


FIG. 2. **Quantifying contextuality by measuring  $\chi_{\text{KSB}}$ .** (A) Measuring  $\chi_{\text{KSB}}$  requires successive quantum non-demolition (QND) measurements of two qubits (Q1, Q2) which we achieve by using an ancilla qubit (An). We construct a long circuit of 180 randomly selected rows or columns (contexts, 540 QND measurements) and run the sequence for 1,000 times. Using single qubit and two qubit entangling gates, a random sequence of rows and columns of Table I is measured and after each measurement the ancilla is reset to the  $|0\rangle$  state. (B) Measuring each row or column (a “context”) entails three successive measurements, each  $\pm 1$ , which in the absence of noise, would multiply to  $+1$  for the rows or  $-1$  for the columns. Plotted are  $6\langle R_i \rangle$  and  $-6\langle C_i \rangle$ , for all rows and columns; error bars indicate  $10 \times$  the statistical uncertainty,  $\sigma$ . The horizontal dashed line corresponding to  $\chi_{\text{KSB}} = 4$  is the classical limit assuming pre-existing classical values of  $\pm 1$  for each of the 9 elements of the table and the olive, horizontal solid line corresponds to the sums of the averages  $\chi_{\text{KSB}} = 5.618 \pm 0.005$ , as given in Eq. (3). Additional data are provided in the Supplementary Materials.

tum mechanics, and the bound that is satisfied by NCHV theories. Consider the set of observables shown in Table I, where observables within each column and each row commute. For any NCHV theory,

$$\chi_{\text{KSB}} = \langle R_1 \rangle + \langle R_2 \rangle + \langle R_3 \rangle - \langle C_1 \rangle - \langle C_2 \rangle - \langle C_3 \rangle \leq 4 \quad (3)$$

where the average is the ensemble average of the products of the outcomes of the observables listed in the first row, and so forth. The above inequality is independent of the preparation of the ensemble, provided all terms are estimated for the same preparation.

In Fig. 2(A) we show a gate sequence that performs QND measurements of the operators in Table I. Each row and column represents a distinct measurement context, and entails three successive measurements, which in theory should multiply to  $+1$  for each row and  $-1$  for each column. We run a circuit with a random sequence of 180 contexts and repeat this sequence 1000 times. The three measurements within each context are also performed in random order. In Fig. 2(B), we show the measured expectation value for each context. The sum of these averages gives  $\chi_{\text{KSB}} = 5.618 \pm 0.005$ , closer to the quantum limit of  $\chi_{\text{KSB}} = 6$  and exceeding previous experiments [15], and significantly above the classical limit of  $\chi_{\text{KSB}} = 4$ . The deviation from 6 is due to various experimental errors in our system (see Supplementary Materials).

It is worth emphasizing the connection between the two experiments presented thus far. Any state-independent proof of strong contextuality can be reformulated as a state-dependent nonlocal game [51–54]. Although our implementations of these two approaches on noisy hardware incur different types of errors, both are well captured by our error-budget analysis. Thus, the observed success probabilities mainly reflect the distinct experimental ingredients and demands of each protocol.

To examine contextuality beyond few-body quantum states, we implement a non-communication game that can be won against classical strategies if the players share an  $N$ -qubit GHZ state [55] before playing the game. This

scalable game provides a natural entry point to many-body condensed-matter settings [56, 57], raising the question of whether such games can certify contextuality in ground states of physical systems.

In the  $N$ -qubit GHZ parity game, there are  $N$  players and each player  $j$  is given a classical bit  $x_j \in \{0, 1\}$ , the “question,” with the promise that  $\sum_j x_j$  is even (Fig. 3(A)). In order to win the game, the players must output bits  $y_j \in \{0, 1\}$  such that

$$\sum_{j=1}^N y_j = \frac{\sum_{j=1}^N x_j}{2} \pmod{2}. \quad (4)$$

If the players do not take advantage of quantum physics, the optimal strategy available to them is random guessing, which wins with a probability  $1/2 + 1/2^{\lfloor N/2 \rfloor}$  (gray line in Fig. 3(B), ref. [57]). If the players instead share the quantum state  $|\text{GHZ}\rangle$  before playing the game, they can win with probability  $P_w = 1$  by measuring their qubits in either the  $X$  or  $Y$  basis, depending on whether their input  $x_j$  is 0 or 1. The players perform the following operations: each applies an  $S$  gate to their qubit if  $x_j = 1$ . Then all players apply the Hadamard gate and measure their qubit in the  $Z$  basis, which gives  $y_j \in \{0, 1\}$ . Since the GHZ state,  $|\text{GHZ}\rangle = (|000\dots\rangle + |111\dots\rangle)/\sqrt{2}$ , is stabilized by a tensor product of Pauli  $X$  and  $Y$  with an even number of  $Y$ , the results will always have even parity.

In Fig. 3(B), we show the results of implementing this algorithm on our superconducting processor up to  $N = 71$  players, where each player corresponds to a qubit. For each choice of the number of players, 20 distinct games (a given set of  $x_j$ ) and 50 choices of qubits for each game are played, where each of these 1000 games is played  $N_s = 1000$  times, and each instance results in a definite win or loss. The winning probability is the average over all games with the indicated standard deviation coming from statistical error in each game. While the measured probability of winning always stays above the classical winning probability, the margin of advantage narrows with

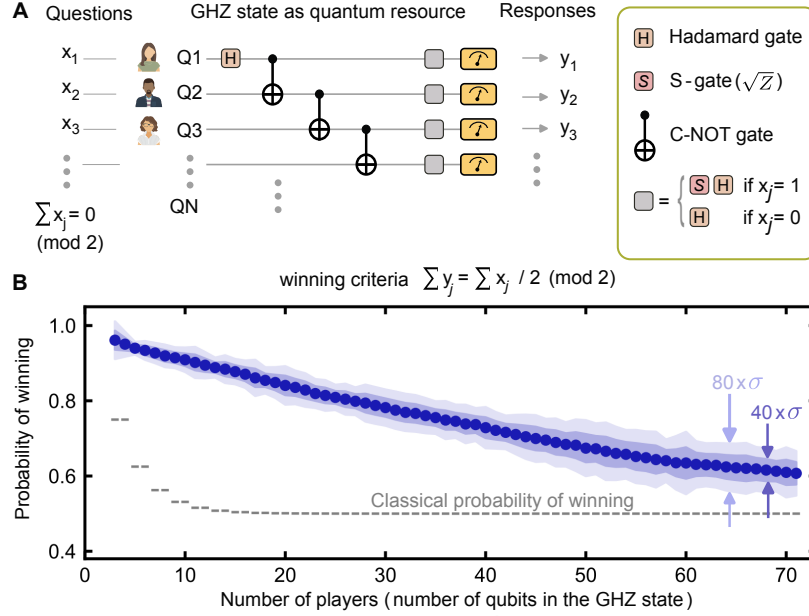


FIG. 3. **The  $N$ -qubit GHZ parity game.** (A) Quantum circuit for the game. Each of the  $N$  players is given a binary value  $x_j$  and is asked to return a binary answer  $y_j$  such that the sum of the answers (mod 2) is the same as the sum of the questions divided by two. Using an  $N$ -qubit GHZ state, players can answer the questions by measuring in a corresponding basis, depending on the binary question ( $x_j$ ) they were assigned. (B) The average winning probability measured on up to 71 qubits (or players). 20 distinct games (a random set of  $x_j$  values) were selected, and each game was implemented on 50 choices of GHZ state growth pattern. Each of these 1000 configurations was measured  $N_s = 1000$  times. The shaded regions are  $\pm 20\sigma$  and  $\pm 40\sigma$  of statistical error computed from the 50 qubit configurations used, after averaging over 20 games played (see Supplementary Materials).

the number of players. Nevertheless, if errors do not systematically favor the  $(|000\dots\rangle - |111\dots\rangle)/\sqrt{2}$  state, playing each game more times reduces the standard deviation of the mean and increases the confidence in outperforming the classical strategy.

Having benchmarked the contextual capabilities of our processor at the many-body level, we now turn to an algorithm with a provable computational advantage. There is a strong equivalence between problems that can be naturally formulated as non-local games and quantum circuits with bounded connectivity [3, 58, 59]. Exploiting this, Bravyi *et al.* gave the first unconditional quantum advantage result for a restricted class of circuits [3]. They considered a family of computational problems and showed that these can be solved exactly by a quantum circuit of fixed constant depth, whereas any classical solution requires logarithmic-depth circuits. Beyond the theoretical proof, it is important to test the noise resilience of such circuits on current quantum processors.

The computational problem that Bravyi *et al.* considered can be viewed as a non-oracular variant of the well-known Bernstein-Vazirani problem [60]. Consider quadratic forms  $q : \{0, 1\}^n \rightarrow \mathbb{Z}_4 = \{0, 1, 2, 3\}$ , defined as

$$q(x) = \sum_{i,j=1}^n A_{i,j} x_i x_j \pmod{4}, \quad (5)$$

where  $x = (x_1, \dots, x_n)$  is a vector of  $n$  binary variables and  $A$  is a symmetric binary matrix. We consider the following hidden linear function (HLF) problem: Given an

$n \times n$  symmetric binary matrix  $A$  specifying a quadratic form  $q(x) = x^T A x$ , which is evaluated modulo 4, find a binary vector  $z \in \{0, 1\}^n$  such that  $q(x) = 2z^T x \pmod{4}$  for all  $x$  in the binary null-space of  $A$ . Bravyi *et al.* devised a quantum algorithm for solving this 2D problem, specializing to the case where  $A_{i,j}$  is nonzero only if  $i$  and  $j$  can be mapped to nearest-neighbors on a 2D grid. They assign each input bit  $A_{i,j}$  to the edge  $\{i, j\}$  and each bit  $A_{i,i}$  at the vertex  $i$  of the 2D grid of qubits. They showed that the 2D HLF problems that are mappable to a 2D square grid of qubits with local gates can be solved with certainty by a shallow quantum circuit.

In Fig. 4(A), we show the gate sequence used for solving a 2D HLF problem for an  $n \times n$  symmetric binary matrix. Qubits are initialized in the  $|0\rangle$  state and then a Hadamard gate is applied to all qubits to create a superposition of all computational states. We focus on a subset of random binary  $n \times n$  matrices  $A$  in which each connectivity-allowed entry is non-zero with probability  $P_{\text{gate}}$ , with all other entries set to zero. To implement the circuit associated with such a matrix, we apply S gates followed by four layers of CZ gates, where S and CZ gates are included whenever the corresponding elements of  $A$  are non-zero. Next, there is a layer of Hadamard gates, followed by a measurement of all qubits, where each measurement instance returns a bitstring that one can verify by comparing against the classical simulation of the quantum circuit. In panel (B), we show the results of measuring  $N_g = 1000$  different choices of  $A$  and measuring each choice  $N_s = 100$  times for matrix size  $n$  values ranging from 9 to 105 qubits.



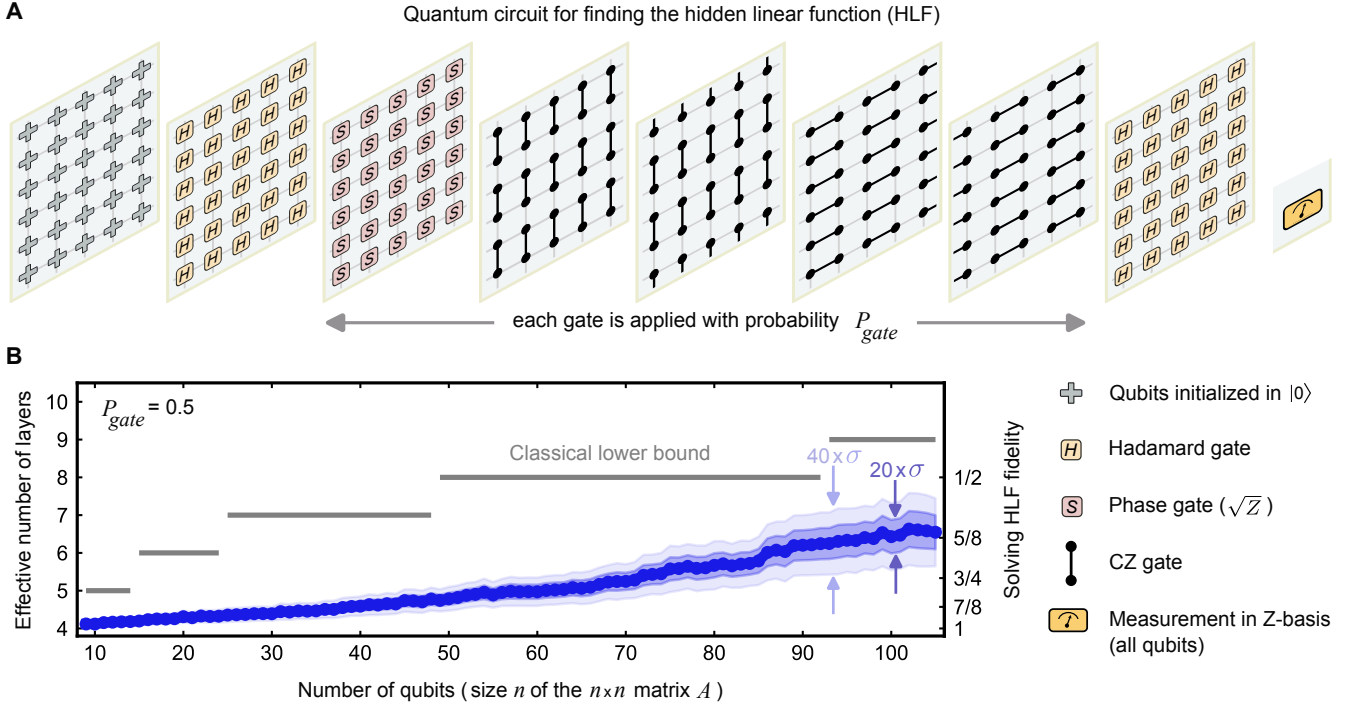


FIG. 4. **Quantum advantage in finding solutions of 2D hidden linear functions.** (A) Quantum circuit for finding a hidden function. Qubits are initialized in a product  $|0\rangle$  state and then a gate is applied to all of them. The encoding of the symmetric  $n \times n$  matrix  $A$  is done by applying an  $S$ -gate where  $A_{i,i}$  is non-zero and CZ-gate between qubits  $i$  and  $j$  where  $A_{i,j}$  is nonzero. The diagonal and allowed off-diagonal elements in  $A$  are non-zero with probability 0.5, where the allowed off-diagonal elements are those which connect neighboring qubits. At the end all qubits are measured in the computational basis, after a layer of Hadamard gates on all qubits. (B) The effective number of layers is defined as 4 divided by the fraction of total number of measured bitstrings that are correct (right axis). Solid data points are the average of  $N_g = 1000$  distinct matrices, each run  $N_s = 100$  times, at each  $n$ -value, and the standard deviation  $\sigma$  is the statistical fluctuations of  $N_g$  distinct runs (see Supplementary Materials for details). The gray horizontal line segments are the classical lower bound.

In the absence of errors, every run of the algorithm returns a correct hidden bitstring. On the quantum processor, errors lead to incorrect outcomes. Comparing measured bitstrings with classical Clifford simulations using Stim [61], we compute the fraction of correct results and define its inverse as an effective two-qubit gate depth for finding the correct bitstring. This metric, sometimes called time-to-solution, quantifies the extra runs needed to find the correct bitstring [62]. In an error-free system, the number of layers remains four at all system sizes, and for smaller  $n$ , the effective depth stays close to this value. As  $n$  grows, the probability of incorrect outcomes increases, raising the effective depth to about six layers for a  $105 \times 105$  matrix.

For the classical circuit depth required to solve the HLF problem, Bravyi *et al.* provide a lower bound for large  $n$ . However, the logarithmic scaling of these bounds implies relevance only for  $n \sim 10^6$  qubits, far beyond current experimental sizes. In the absence of a theoretical lower bound for near-term devices, we conjecture that for a function depending on all  $s$  inputs, the minimum classical circuit depth required to implement a Boolean function using two-input, one-output gates is  $\log_2(s)$  for an *exact* solution to the HLF problem. This formula counts the number of two-bit gate layers a classical computer needs to find a bitstring of length  $n$ , without constrain-

ing circuit connectivity. We plot these bounds as gray lines in Fig. 4(B), which exceed our quantum results, suggesting that the problem is effectively solved with fewer two-qubit gate layers on our quantum processor than the two-bit gate layers required in the classical circuit model.

In this work, we leveraged the flexibility of a large 2D array of superconducting qubits to show that many-body quantum contextuality can enable bounded-resource tasks more efficiently than classical counterparts. At the few-qubit level, we implemented the Mermin-Peres game and violated a Kochen-Specker-Bell inequality, achieving record performance where the maximum attainable contextuality, rather than merely a lower-bound violation, becomes the target. Extending to scalable many-body tasks, we demonstrated contextual behavior by outperforming classical strategies using up to 105 qubits. The sensitivity of these many-body algorithms also allowed us to benchmark our processor and detect subtle coherent errors absent in random unitary operations. To guide hardware development and reduce the performance gap from the noiseless quantum expectation, we propose using many-body contextuality as a benchmark for future quantum devices.

**Acknowledgment.** We thank Č. Brukner, V. B. Bulchandani, F. Burnell, A. Cabello, B. Dakić, C. A.

Fuchs, R. M. Nandkishore, N. Medina Sanchez, S. L. Sondhi, and R. Spekkens for insightful discussions.

<sup>†</sup> Google Quantum AI

S. Kumar<sup>1,2,†</sup>, E. Rosenberg<sup>1,†</sup>, A. Grajales Dau<sup>1,†</sup>, R. G. Cortiñas<sup>1,†</sup>, D. Maslov<sup>1</sup>, R. Oliver<sup>1</sup>, A. Zalcman<sup>1</sup>, M. Neeley<sup>1</sup>, A. Pagano<sup>1</sup>, A. Szasz<sup>1</sup>, I. Drozdov<sup>1</sup>, Z. Mineev<sup>1</sup>, C. Gidney<sup>1</sup>, N. Yosri<sup>1</sup>, S. J. de Graaf<sup>1</sup>, A. Maiti<sup>1</sup>, D. Abanin<sup>1</sup>, R. Acharya<sup>1</sup>, L. Aghababaie Beni<sup>1</sup>, G. Aigeldinger<sup>1</sup>, R. Alcaraz<sup>1</sup>, S. Alcaraz<sup>1</sup>, T. I. Andersen<sup>1</sup>, M. Ansmann<sup>1</sup>, F. Arute<sup>1</sup>, K. Arya<sup>1</sup>, W. Askew<sup>1</sup>, N. Astrakhantsev<sup>1</sup>, J. Atalaya<sup>1</sup>, R. Babbush<sup>1</sup>, B. Ballard<sup>1</sup>, J. C. Bardin<sup>1,4</sup>, H. Bates<sup>1</sup>, A. Bengtsson<sup>1</sup>, M. Bigdeli Karimi<sup>1</sup>, A. Bilmes<sup>1</sup>, S. Bilodeau<sup>1</sup>, F. Borjans<sup>1</sup>, A. Bourassa<sup>1</sup>, J. Bovaird<sup>1</sup>, D. Bowers<sup>1</sup>, L. Brill<sup>1</sup>, P. Brooks<sup>1</sup>, M. Broughton<sup>1</sup>, D. A. Browne<sup>1</sup>, B. Buchea<sup>1</sup>, B. B. Buckley<sup>1</sup>, T. Burger<sup>1</sup>, B. Burkett<sup>1</sup>, N. Bushnell<sup>1</sup>, J. Busnaina<sup>1</sup>, A. Cabrera<sup>1</sup>, J. Campero<sup>1</sup>, H.-S. Chang<sup>1</sup>, S. Chen<sup>1</sup>, Z. Chen<sup>1</sup>, B. Chiaro<sup>1</sup>, L.-Y. Chih<sup>1</sup>, J. Claes<sup>1</sup>, A. Y. Cleland<sup>1</sup>, B. Cochrane<sup>1</sup>, M. Cockrell<sup>1</sup>, J. Cogan<sup>1</sup>, R. Collins<sup>1</sup>, P. Conner<sup>1</sup>, H. Cook<sup>1</sup>, W. Courtney<sup>1</sup>, A. L. Crook<sup>1</sup>, B. Curtin<sup>1</sup>, S. Das<sup>1</sup>, S. Demura<sup>1</sup>, L. De Lorenzo<sup>1</sup>, A. Di Paolo<sup>1</sup>, P. Donohoe<sup>1</sup>, A. Dunsworth<sup>1</sup>, V. Ehimhen<sup>1</sup>, A. Eickbusch<sup>1</sup>, A. Moshe Elbag<sup>1</sup>, L. Ella<sup>1</sup>, M. Elzouka<sup>1</sup>, D. Enriquez<sup>1</sup>, C. Erickson<sup>1</sup>, V. S. Ferreira<sup>1</sup>, M. Flores<sup>1</sup>, L. Flores Burgos<sup>1</sup>, E. Forati<sup>1</sup>, J. Ford<sup>1</sup>, B. Foxen<sup>1</sup>, M. Fukami<sup>1</sup>, A. W. L. Fung<sup>1</sup>, L. Fuste<sup>1</sup>, S. Ganjam<sup>1</sup>, G. Garcia<sup>1</sup>, C. Garrick<sup>1</sup>, R. Gasca<sup>1</sup>, H. Gehring<sup>1</sup>, É. Genois<sup>1</sup>, W. Giang<sup>1</sup>, D. Gilboa<sup>1</sup>, J. E. Goeders<sup>1</sup>, E. Gonzales<sup>1</sup>, R. Gosula<sup>1</sup>, D. Graumann<sup>1</sup>, J. Grebel<sup>1</sup>, A. Greene<sup>1</sup>, J. A. Gross<sup>1</sup>, J. Guerrero<sup>1</sup>, T. Ha<sup>1</sup>, S. Habegger<sup>1</sup>, T. Hadick<sup>1</sup>, M. Hansen<sup>1</sup>, M. P. Harrigan<sup>1</sup>, S. D. Harrington<sup>1</sup>, J. Hartshorn<sup>1</sup>, S. Heslin<sup>1</sup>, P. Heu<sup>1</sup>, O. Higgott<sup>1</sup>, R. Hiltermann<sup>1</sup>, J. Hilton<sup>1</sup>, H.-Y. Huang<sup>1</sup>, M. Hucka<sup>1</sup>, A. Huff<sup>1</sup>, W. J. Huggins<sup>1</sup>, E. Jeffrey<sup>1</sup>, S. Jevons<sup>1</sup>, Z. Jiang<sup>1</sup>, X. Jin<sup>1</sup>, C. Jones<sup>1</sup>, C. Joshi<sup>1</sup>, P. Juhas<sup>1</sup>, A. Kabel<sup>1</sup>, D. Kafri<sup>1</sup>, H. Kang<sup>1</sup>, A. H. Karamlou<sup>1</sup>, R. Kaufman<sup>1</sup>, K. Kechedzhi<sup>1</sup>, T. Khaira<sup>1</sup>, T. Khattar<sup>1</sup>, M. Khezri<sup>1</sup>, S. Kim<sup>1</sup>, P. V. Klimov<sup>1</sup>, C. M. Knaut<sup>1</sup>, B. Kobrin<sup>1</sup>, A. N. Korotkov<sup>1</sup>, F. Kostriksa<sup>1</sup>, J. M. Kreikebaum<sup>1</sup>, R. Kudo<sup>1</sup>, B. Kueffler<sup>1</sup>, A. Kumar<sup>1</sup>, V. D. Kurilovich<sup>1</sup>, V. Kutsko<sup>1</sup>, D. Landhuis<sup>1</sup>, T. Lange-Dei<sup>1</sup>, B. W. Langley<sup>1</sup>, P. Laptev<sup>1</sup>, K.-M. Lau<sup>1</sup>, E. Leavell<sup>1</sup>, J. Ledford<sup>1</sup>, J. Lee<sup>1</sup>, K. Lee<sup>1</sup>, B. J. Lester<sup>1</sup>, W. Leung<sup>1</sup>, L. Le Guevel<sup>1</sup>, L. Li<sup>1</sup>, W. Y. Li<sup>1</sup>, A. T. Lill<sup>1</sup>, W. P. Livingston<sup>1</sup>, M. T. Lloyd<sup>1</sup>, A. Locharla<sup>1</sup>, D. Lundahl<sup>1</sup>, A. Lunt<sup>1</sup>, S. Madhuk<sup>1</sup>, A. Maloney<sup>1</sup>, S. Mandrà<sup>1</sup>, L. S. Martin<sup>1</sup>, O. Martin<sup>1</sup>, E. Mascot<sup>1</sup>, P. Masih Das<sup>1</sup>, C. Maxfield<sup>1</sup>, J. R. McClean<sup>1</sup>, M. McEwen<sup>1</sup>, S. Meeks<sup>1</sup>, A. Megrant<sup>1</sup>, K. C. Miao<sup>1</sup>, R. Molavi<sup>1</sup>, S. Molina<sup>1</sup>, S. Montazeri<sup>1</sup>, C. Neill<sup>1</sup>, M. Newman<sup>1</sup>, A. Nguyen<sup>1</sup>, M. Nguyen<sup>1</sup>, C.-H. Ni<sup>1</sup>, M. Y. Niu<sup>1</sup>, L. Oas<sup>1</sup>, W. D. Oliver<sup>1</sup>, R. Orosco<sup>1</sup>, K. Ottosson<sup>1</sup>, S. Peek<sup>1</sup>, D. Peterson<sup>1</sup>, A. Pizzuto<sup>1</sup>, R. Potter<sup>1</sup>, O. Pritchard<sup>1</sup>, M. Qian<sup>1</sup>, C. Quintana<sup>1</sup>, G. Ramachandran<sup>1</sup>, A. Ranadive<sup>1</sup>, M. J. Reagor<sup>1</sup>, R. Resnick<sup>1</sup>, D. M. Rhodes<sup>1</sup>, D. Riley<sup>1</sup>, G. Roberts<sup>1</sup>, R. Rodriguez<sup>1</sup>, E. Ropes<sup>1</sup>, E. Rosenfeld<sup>1</sup>, D. Rosenstock<sup>1</sup>, E. Rossi<sup>1</sup>, D. A. Rower<sup>1</sup>, K. Sankaragomathi<sup>1</sup>, M. C. Sarihan<sup>1</sup>, K. J. Satzinger<sup>1</sup>, S. Schroeder<sup>1</sup>, H. F. Schurkus<sup>1</sup>, A. Shahingohar<sup>1</sup>, M. J. Shearn<sup>1</sup>, A. Shorter<sup>1</sup>, N. Shutty<sup>1</sup>, V. Shvarts<sup>1</sup>, V. Sivak<sup>1</sup>, S. Small<sup>1</sup>, W. C. Smith<sup>1</sup>, D. A. Sobel<sup>1</sup>, B. Spells<sup>1</sup>, S. Springer<sup>1</sup>, G. Sterling<sup>1</sup>, J. Suchard<sup>1</sup>, A. Szein<sup>1</sup>, M. Taylor<sup>1</sup>, J. P. Thiruraman<sup>1</sup>, D. Thor<sup>1</sup>, D. Timucin<sup>1</sup>, E. Tomita<sup>1</sup>, A. Torres<sup>1</sup>, M. M. Torunbalci<sup>1</sup>, H. Tran<sup>1</sup>, A. Vaishnav<sup>1</sup>, J. Vargas<sup>1</sup>, S. Vdovichev<sup>1</sup>, G. Vidal<sup>1</sup>, C. Vollgraft Heidweiller<sup>1</sup>, M. Voorhees<sup>1</sup>, S. Waltman<sup>1</sup>, J. Waltz<sup>1</sup>, S. X. Wang<sup>1</sup>, B. Ware<sup>1</sup>, J. D. Watson<sup>1</sup>, T. Weidel<sup>1</sup>, T. White<sup>1</sup>, K. Wong<sup>1</sup>, B. W. K. Woo<sup>1</sup>, C. J. Wood<sup>1</sup>, M. Woodson<sup>1</sup>, C. Xing<sup>1</sup>, Z. J. Yao<sup>1</sup>, P. Yeh<sup>1</sup>, B. Ying<sup>1</sup>, J. Yoo<sup>1</sup>, E. Young<sup>1</sup>, G. Young<sup>1</sup>, R. Zhang<sup>1</sup>, Y. Zhang<sup>1</sup>, N. Zhu<sup>1</sup>, N. Zobrist<sup>1</sup>, Z. Zou<sup>1</sup>, S. Puri<sup>1,3</sup>, E. Lucero<sup>1</sup>, J. Kelly<sup>1</sup>, S. Boixo<sup>1</sup>, Y. Chen<sup>1</sup>, V. Smelyanskiy<sup>1</sup>, H. Neven<sup>1</sup>, P. Roushan<sup>1,§</sup>, M. Devoret<sup>1,5,§</sup>

<sup>1</sup> Google Research, Mountain View, CA, USA

<sup>2</sup> Department of Electrical and Computer Engineering, Princeton University, Princeton, NJ, USA

<sup>3</sup> Department of Applied Physics, Yale University, New Haven, CT, USA

<sup>4</sup> Department of Electrical and Computer Engineering, University of Massachusetts, Amherst, MA

<sup>5</sup> Department of Physics, University of California, Santa Barbara, CA

<sup>6</sup> Department of Electrical and Computer Engineering, University of California, Riverside, CA

<sup>7</sup> Pritzker School of Molecular Engineering, University of Chicago, Chicago, IL

<sup>8</sup> Department of Physics and Astronomy, University of California, Riverside, CA

<sup>9</sup> Department of Electrical and Computer Engineering, Auburn University, Auburn, AL

<sup>†</sup> These authors contributed equally to this work.

<sup>§</sup> Corresponding author: pedramr@google.com

<sup>§</sup> Corresponding author: devoret@google.com

- 
- [1] R. Raussendorf, Contextuality in measurement-based quantum computation, *Phys. Rev. A* **88**, 022322 (2013).
- [2] M. Howard *et al.*, Contextuality supplies the ‘magic’ for quantum computation, *Nature* **510**, 351 (2014).
- [3] S. Bravyi *et al.*, Quantum advantage with shallow circuits, *Science* **362**, 308 (2018).
- [4] S. Bravyi *et al.*, Quantum advantage with noisy shallow circuits, *Nature Physics* **16**, 1040 (2020).
- [5] M. Coudron, J. Stark, and T. Vidick, Trading locality for time: certifiable randomness from low-depth circuits, *Commun. Math. Phys.* **382**, 49 (2021).
- [6] A. Watts *et al.*, Exponential separation between shallow quantum circuits and unbounded fan-in shallow classical circuits, in *Proceedings of the 51st Annual ACM SIGACT Symposium on Theory of Computing* (2019) pp. 515–526.
- [7] D. Grier and L. Schaeffer, Interactive shallow Clifford circuits: Quantum advantage against NC<sup>1</sup> and beyond, in *Proceedings of the 52nd Annual ACM SIGACT Symposium on Theory of Computing* (2020) pp. 875–888.
- [8] W. Kretschmer, S. Grewal, M. DeCross, J. A. Gerber, K. Gilmore, D. Gresh, N. Hunter-Jones, K. Mayer, B. Neyenhuis, D. Hayes, *et al.*, Demonstrating an unconditional separation between quantum and classical information resources, arXiv preprint arXiv:2509.07255 (2025).
- [9] D.-L. Deng, C. Wu, J.-L. Chen, S.-J. Gu, S. Yu, and C. H. Oh, Bell nonlocality in conventional and topological quantum phase transitions, *Phys. Rev. A* **86**, 032305 (2012).
- [10] J. Tura, R. Augusiak, A. B. Sainz, T. Vértesi, M. Lewenstein, and A. Acín, Detecting nonlocality in many-body quantum states, *Science* **344**, 1256 (2014).
- [11] R. Schmied, J.-D. Bancal, B. Allard, M. Fadel, V. Scarani, P. Treutlein, and N. Sangouard, Bell correlations in a Bose-Einstein condensate, *Science* **352**, 441 (2016).
- [12] S. Pelisson, L. Pezzè, and A. Smerzi, Coherence visibility as a witness of quantum correlations, *Phys. Rev. A* **93**, 022115 (2016).

- [13] J. Tura, G. D. las Cuevas, R. Augusiak, M. Lewenstein, A. Acín, and J. I. Cirac, Energy as a detector of nonlocality of many-body spin systems, *Phys. Rev. X* **7**, 021005 (2017).
- [14] A. K. Daniel and A. Miyake, Quantum computational advantage with string order parameters of one-dimensional symmetry-protected topological order, *Phys. Rev. Lett.* **126**, 090505 (2021).
- [15] G. Kirchmair *et al.*, State-independent experimental test of quantum contextuality, *Nature* **460**, 494 (2009).
- [16] O. Moussa *et al.*, Testing contextuality on quantum ensembles with one clean qubit, *Phys. Rev. Lett.* **104**, 160501 (2010).
- [17] X. Zhang *et al.*, State-independent experimental test of quantum contextuality with a single trapped ion, *Phys. Rev. Lett.* **110**, 070401 (2013).
- [18] X. Hu *et al.*, Experimental Test of Compatibility-Loophole-Free Contextuality with Spatially Separated Entangled Qutrits, *Phys. Rev. Lett.* **117**, 170403 (2016).
- [19] M. Jerger *et al.*, Contextuality without nonlocality in a superconducting quantum system, *Nature Communications* **7**, 12930 (2016).
- [20] F. M. Leupold *et al.*, Sustained state-independent quantum contextual correlations from a single ion, *Phys. Rev. Lett.* **120**, 180401 (2018).
- [21] S. van Dam *et al.*, Multipartite entanglement generation and contextuality tests using nondestructive three-qubit parity measurements, *Phys. Rev. Lett.* **123**, 050401 (2019).
- [22] F. Holweck, Testing quantum contextuality of binary symplectic polar spaces on a noisy intermediate scale quantum computer, *Quantum Information Processing* **20**, 247 (2021).
- [23] P. Wang *et al.*, Significant loophole-free test of Kochen-Specker contextuality using two species of atomic ions, *Science Advances* **8**, eabk1660 (2022).
- [24] J.-M. Xu *et al.*, Experimental Demonstration of Quantum Pseudotelepathy, *Phys. Rev. Lett.* **129**, 050402 (2022).
- [25] A. Laghaout *et al.*, A demonstration of contextuality using quantum computers, *European Journal of Physics* **43**, 055401 (2022).
- [26] P. Xue, L. Xiao, G. Ruffolo, A. Mazzari, T. Temistocles, M. T. Cunha, and R. Rabelo, Synchronous observation of Bell nonlocality and state-dependent contextuality, *Phys. Rev. Lett.* **130**, 040201 (2023).
- [27] M. Fabbrichesi *et al.*, Tests of quantum contextuality in particle physics, *arXiv preprint arXiv:2504.12382* (2025).
- [28] C. Kelleher and F. Holweck, Empirical demonstration of quantum contextuality on nisq computers, *arXiv preprint arXiv:2505.21243* (2025).
- [29] R. W. Spekkens, Negativity and contextuality are equivalent notions of nonclassicality, *Phys. Rev. Lett.* **101**, 020401 (2008).
- [30] S. Abramsky and A. Brandenburger, The sheaf-theoretic structure of non-locality and contextuality, *New Journal of Physics* **13**, 113036 (2011).
- [31] A. Pais, Einstein and the quantum theory, *Rev. Mod. Phys.* **51**, 863 (1979).
- [32] N. D. Mermin, Is the moon there when nobody looks? reality and the quantum theory, *Physics Today* **38**, 38 (1985).
- [33] A. Einstein, B. Podolsky, and N. Rosen, Can quantum-mechanical description of physical reality be considered complete?, *Phys. Rev.* **47**, 777 (1935).
- [34] S. J. Freedman and J. F. Clauser, Experimental test of local hidden-variable theories, *Phys. Rev. Lett.* **28**, 938 (1972).
- [35] A. Aspect, J. Dalibard, and G. Roger, Experimental test of Bell's inequalities using time-varying analyzers, *Phys. Rev. Lett.* **49**, 1804 (1982).
- [36] N. D. Mermin, Extreme quantum entanglement in a superposition of macroscopically distinct states, *Phys. Rev. Lett.* **65**, 1838 (1990).
- [37] D. Greenberger, M. Horne, A. Shimony, and A. Zeilinger, Bell's Theorem without Inequalities, *American Journal of Physics* **58**, 1131 (1990).
- [38] G. Brassard, A. Broadbent, and A. Tapp, Multi-party pseudo-telepathy, in *Workshop on Algorithms and Data Structures* (Springer, 2003) pp. 1–11.
- [39] G. Brassard, A. Broadbent, and A. Tapp, Quantum pseudo-telepathy, *Foundations of Physics* **35**, 1877 (2005).
- [40] N. D. Mermin, Simple unified form for the major no-hidden-variables theorems, *Phys. Rev. Lett.* **65**, 3373 (1990).
- [41] A. Peres, Incompatible results of quantum measurements, *Phys. Lett. A* **151**, 107 (1990).
- [42] A. Cabello, Bell's theorem without inequalities and without probabilities for two observers, *Phys. Rev. Lett.* **86**, 1911 (2001).
- [43] A. Cabello, "All versus nothing" inseparability for two observers, *Phys. Rev. Lett.* **87**, 010403 (2001).
- [44] P. Aravind, A simple demonstration of Bell's theorem involving two observers and no probabilities or inequalities, *arXiv:quant-ph/0206070* (2002).
- [45] E. P. Specker, Die Logik nicht gleichzeitig entscheidbarer Aussagen, *Dialectica* **14**, 239 (1960).
- [46] J. S. Bell, On the problem of hidden variables in quantum mechanics, *Rev. Mod. Phys.* **38**, 447 (1966).
- [47] S. Kochen and E. Specker, The problem of hidden variables in quantum mechanics, *Journal of Mathematics and Mechanics* **17**, 59 (1967).
- [48] N. D. Mermin, Hidden variables and the two theorems of John Bell, *Rev. Mod. Phys.* **65**, 803 (1993).
- [49] A. Cabello, Experimentally testable state-independent quantum contextuality, *Phys. Rev. Lett.* **101**, 210401 (2008).
- [50] P. Badziąg *et al.*, Universality of state-independent violation of correlation inequalities for noncontextual theories, *Phys. Rev. Lett.* **103**, 050401 (2009).
- [51] P. Heywood and M. L. G. Redhead, Nonlocality and the kochen-specker paradox, *Foundations of Physics* **13**, 481 (1983).
- [52] P. K. Aravind, Bell's theorem without inequalities and only two distant observers, *Foundations of Physics Letters* **15**, 397 (2002).
- [53] S. Abramsky, R. S. Barbosa, N. De Silva, and O. Zapata, The quantum monad on relational structures, *arXiv preprint arXiv:1705.07310* (2017).
- [54] A. Cabello, Converting contextuality into nonlocality, *Physical Review Letters* **127**, 070401 (2021).
- [55] D. M. Greenberger, M. A. Horne, and A. Zeilinger, Going Beyond Bell's Theorem, in *Bell's Theorem, Quantum Theory and Conceptions of the Universe*, edited by M. Kafatos (Springer Netherlands, Dordrecht, 1989) pp. 69–72.
- [56] V. B. Bulchandani, F. J. Burnell, and S. L. Sondhi, A multiplayer multiteam nonlocal game for the toric code, *Phys. Rev. B* **107**, 035409 (2023).
- [57] V. B. Bulchandani, F. J. Burnell, and S. L. Sondhi, Playing nonlocal games with phases of quantum matter, *Phys. Rev. B* **107**, 045412 (2023).
- [58] S. Aasnaess, *Comparing two cohomological obstructions* (1972).

- tions for contextuality, and a generalised construction of quantum advantage with shallow circuits (2022), [arXiv:2212.09382 \[quant-ph\]](#).
- [59] C. Vieira, R. Ramanathan, and A. Cabello, Test of the physical significance of bell nonlocality, *Nature Communications* **16**, 4390 (2025).
  - [60] E. Bernstein and U. Vazirani, Quantum complexity theory, in *Proceedings of the 25th Annual ACM Symposium on Theory of Computing (STOC)* (ACM, 1993) pp. 11–20.
  - [61] C. Gidney, Stim: a fast stabilizer circuit simulator, *Quantum* **5**, 497 (2021).
  - [62] B. Pokharel and D. A. Lidar, Demonstration of algorithmic quantum speedup, *Phys. Rev. Lett.* **130**, 210602 (2023).
  - [63] R. Acharya *et al.*, Quantum error correction below the surface code threshold, *Nature* **638**, 920 (2025).
  - [64] P. V. Klimov, A. Bengtsson, C. Quintana, A. Bourassa, S. Hong, A. Dunsworth, K. J. Satzinger, W. P. Livingston, V. Sivak, M. Y. Niu, T. I. Andersen, Y. Zhang, D. Chik, Z. Chen, C. Neill, C. Erickson, A. Grajales Dau, A. Megrant, P. Roushan, A. N. Korotkov, J. Kelly, V. Smelyanskiy, Y. Chen, and H. Neven, Optimizing quantum gates towards the scale of logical qubits, *Nature Communications* **15**, 2442 (2024).
  - [65] A. Bengtsson, A. Opremcak, M. Khezri, D. Sank, A. Bourassa, K. J. Satzinger, S. Hong, C. Erickson, B. J. Lester, K. C. Miao, A. N. Korotkov, J. Kelly, Z. Chen, and P. V. Klimov, Model-based optimization of superconducting qubit readout, *Phys. Rev. Lett.* **132**, 100603 (2024).
  - [66] Cirq Developers, *Cirq* (2024).
  - [67] E. H. Chen, G.-Y. Zhu, R. Verresen, A. Seif, E. Bäumer, D. Layden, N. Tantivasadakarn, G. Zhu, S. Sheldon, A. Vishwanath, *et al.*, Nishimori transition across the error threshold for constant-depth quantum circuits, *Nature Physics* **21**, 161 (2025).
  - [68] S. T. Flammia and Y.-K. Liu, Direct fidelity estimation from few pauli measurements, *Phys. Rev. Lett.* **106**, 230501 (2011).
  - [69] T. H. Cormen, C. E. Leiserson, R. L. Rivest, and C. Stein, *Introduction to Algorithms* (MIT press, 2022).



**Supplementary Materials for  
“Quantum–Classical Separation in Bounded-Resource Tasks Arising from Measurement  
Contextuality”**

Google Quantum AI<sup>†</sup>

**CONTENTS**

|                                                                 |    |
|-----------------------------------------------------------------|----|
| 1. List of Symbols                                              | 10 |
| 2. Device Characterization                                      | 11 |
| 3. Mermin-Peres Magic Square Game: Variations and Error Budget  | 12 |
| 4. Kochen-Specker-Bell Inequality: Further Data and Calibration | 14 |
| 4.A. Continuous Measurement of a Random Sequence                | 14 |
| 4.B. Calibrating Compensation Phases                            | 15 |
| 5. GHZ State: Fidelity and Error Estimation                     | 16 |
| 5.A. Fidelity                                                   | 16 |
| a. Definition                                                   | 16 |
| b. Stabilizers                                                  | 17 |
| 5.B. Error Estimation                                           | 17 |
| a. Fidelity under $T_1$ with Dynamical Decoupling               | 17 |
| b. Fidelity under Single-Qubit Gates                            | 19 |
| c. Fidelity under Two-Qubit Gates                               | 19 |
| d. Fidelity under Readout Error                                 | 19 |
| 5.C. GHZ State Growth and Fidelity                              | 21 |
| 6. Shallow Circuits and Hidden Linear Function (HLF) Problem    | 22 |
| 6.A. Formalism and Further Experimental Data                    | 22 |
| 6.B. Lower Bound Analysis                                       | 23 |

## 1. LIST OF SYMBOLS

| Symbol                                                                       | Description                                                                               |
|------------------------------------------------------------------------------|-------------------------------------------------------------------------------------------|
| $N$                                                                          | Number of qubits in the GHZ state                                                         |
| $ \text{GHZ}\rangle$                                                         | $N$ -qubit GHZ state, $\frac{1}{\sqrt{2}}( 0\rangle^{\otimes N} +  1\rangle^{\otimes N})$ |
| $\tilde{\rho}_{\text{GHZ}}$                                                  | Experimentally prepared GHZ state                                                         |
| $F$                                                                          | Fidelity of $\tilde{\rho}_{\text{GHZ}}$ with respect to $ \text{GHZ}\rangle$              |
| $\hat{P}_i$                                                                  | $N$ -qubit Pauli operator                                                                 |
| $\{\hat{S}_i\}$                                                              | Set of $2^N$ stabilizers of $ \text{GHZ}\rangle$                                          |
| $\hat{Q}_i$                                                                  | Generator of the stabilizer group                                                         |
| $F^X, F^Z$                                                                   | Fidelities associated with $X$ -type and $Z$ -type stabilizers                            |
| $F_{T_1}$                                                                    | Fidelity of GHZ state under $T_1$ decay                                                   |
| $n_{\text{sq}}$                                                              | Number of single-qubit gates                                                              |
| $e_p^{\text{sq}}$                                                            | Pauli error probability per single-qubit gate                                             |
| $F_{\text{sq}}, F_{\text{sq}}^X, F_{\text{sq}}^Z$                            | Total, $X$ -type, and $Z$ -type fidelities from single-qubit errors                       |
| $n_{2\text{q}}$                                                              | Number of two-qubit gates                                                                 |
| $e_p^{2\text{q}}$                                                            | Pauli error probability per two-qubit gate                                                |
| $F_{2\text{q}}, F_{2\text{q}}^X, F_{2\text{q}}^Z$                            | Fidelities from two-qubit gate errors                                                     |
| $n_{\text{ro}}$                                                              | Number of measurement gates                                                               |
| $e_0, e_1$                                                                   | Probabilities of misidentifying $ 0\rangle,  1\rangle$ in readout                         |
| $\varepsilon$                                                                | Symmetric readout error rate ( $e_0 = e_1 = \varepsilon$ )                                |
| $Z_\Lambda, X_\Lambda, Y_\Lambda$                                            | Transformed observables under readout noise                                               |
| $F_{\text{readout,asym}}$                                                    | Fidelity under asymmetric readout error                                                   |
| $F_{\text{readout,sym}}, F_{\text{readout,sym}}^X, F_{\text{readout,sym}}^Z$ | Fidelities under symmetric readout error                                                  |
| $F_{\text{total}}$                                                           | Total GHZ fidelity including all error channels                                           |
| $P_w$                                                                        | Winning probability of the bounded-resource task                                          |
| $N_g$                                                                        | Number of randomized GHZ game or HLF instances                                            |
| $N_s$                                                                        | Number of shots (repetitions) per instance                                                |
| $SD_{50}, SD_{1000}$                                                         | Standard deviation across 50 GHZ or 1000 HLF instances                                    |
| $L_{\text{classical}}$                                                       | Lower bound on classical circuit depth                                                    |
| $A$                                                                          | $n \times n$ matrix defining the 2D HLF problem                                           |
| $S$                                                                          | Phase gate ( $\sqrt{Z}$ ) used in the HLF encoding                                        |
| $\text{CZ}$                                                                  | Controlled- $Z$ gate (native two-qubit entangling operation)                              |
| $P_{\text{gate}}$                                                            | Probability of applying each allowed $S$ or $\text{CZ}$ gate in the 2D HLF problem        |

## 2. DEVICE CHARACTERIZATION

The experiments were performed on 72-qubit and 105-qubit Willow processors, with architectures similar to those described in Ref. [63]. In all cases, CZ gates served as the native entangling operation. Fig. S1 shows representative error rates for a 71-qubit grid on the 72-qubit processor and a 105-qubit grid on the 105-qubit processor. Details of gate optimization are provided in Refs. [64, 65].

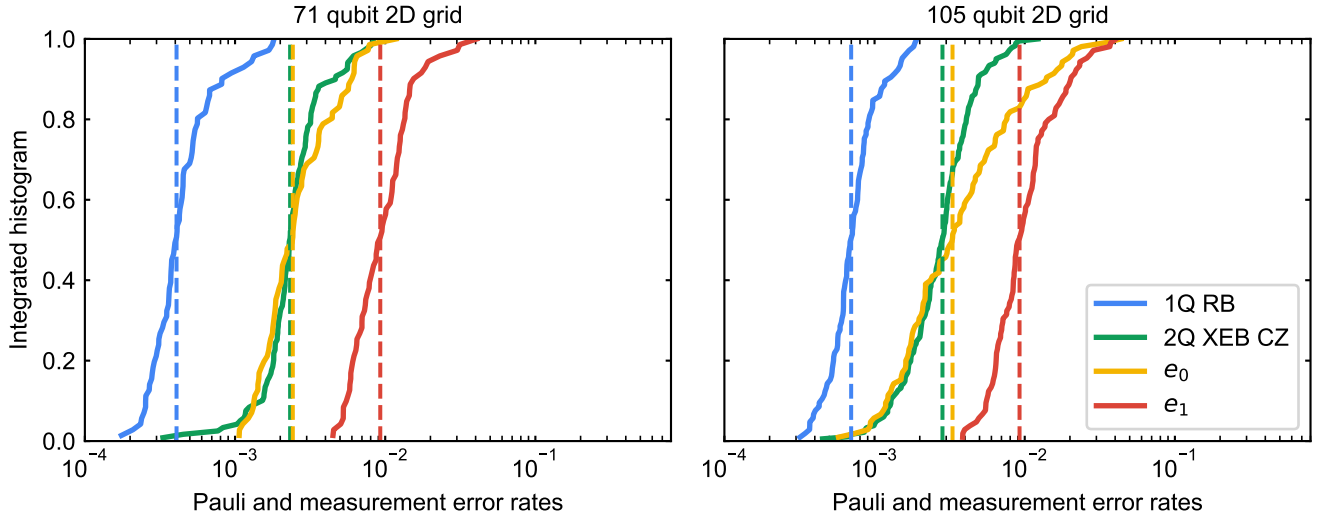


FIG. S1. **Representative error rates for a 71-qubit 2D grid on the 72-qubit Willow processor and a 105-qubit 2D grid on the 105-qubit Willow processor.** The data include readout (measurement) errors, single-qubit randomized benchmarking (1Q RB) errors, and two-qubit cross-entropy benchmarking (2Q XEB) Pauli errors for CZ gates. Vertical dashed lines denote the median values for each dataset. The readout errors  $e_0$  and  $e_1$  correspond to the probability of reporting  $|1\rangle$  when the qubit is prepared in  $|0\rangle$  and of reporting  $|0\rangle$  when prepared in  $|1\rangle$ , respectively.

### 3. MERMIN-PERES MAGIC SQUARE GAME: VARIATIONS AND ERROR BUDGET

When using quantum resources, the Mermin-Peres square game can be played in several different ways that would all be equivalent in the absence of noise:

- **Variation I.** Alice and Bob decide to measure only two of the three Pauli operators corresponding to their assigned row and column. They then each infer the outcome of the third Pauli such that the product of the three results equals  $+1$  for Alice (assigned to rows) and  $-1$  for Bob (assigned to columns). This is the strategy that is used in Figure 1 of the main text.
- **Variation II.** In this version, they do not compute the third Pauli outcome but measure it directly on the processor (Fig. S2). Consequently, the circuits become larger to accommodate the third Pauli measurement. Each player uses two ancilla qubits to measure two Paulis and employs their half of the Bell pair to measure the third Pauli. This circuit construction is not unique and could alternatively be done with one ancilla. Either the rules of the game or the strategy utilized by Alice and Bob must be modified to accommodate cases where the three measurements do not multiply correctly (which was stipulated as a rule in the original formulation of the game), but here we focus on presenting the experimental data itself rather than discussing the implications of variations of the game's rules.

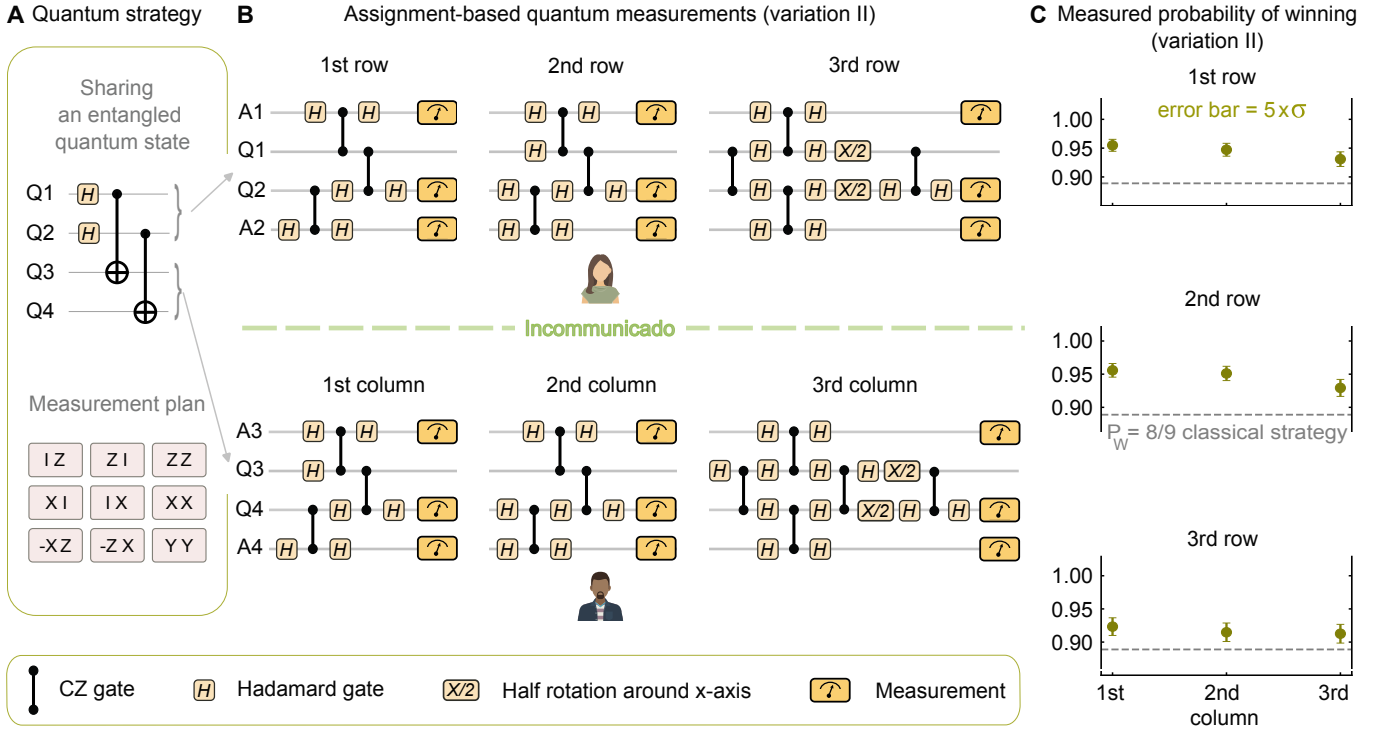


FIG. S2. **Variation II of the Mermin-Peres magic square game.** (A) Players share two Bell pairs and agree on the measurement basis for each assigned row (Alice) or column (Bob). (B) Using ancilla qubits, each player performs three simultaneous measurements corresponding to their assigned row or column. For clarity, we omit the dynamical decoupling sequences applied to qubits during idle periods. We also depict the circuits using CZ, Hadamard, and  $X/2$  gates, although in the actual implementation, contiguous single-qubit gates are compiled into a single operation. (C) Measured probability that both players follow their respective multiplication rules and obtain matching outcomes in the shared cell, shown for nine distinct games (row-column assignments) sorted by the position of their intersection. The average win probability is  $P_w = 0.9355 \pm 0.0008$ . Each game is played  $N_s = 10,000$  times, and the error bar for each game is five times the statistical uncertainty derived from the binomial distribution.

Figure S3(A) shows the measured win probabilities for Variations I and II. Panel (B) presents the estimated error budget for both variations, in agreement with the average measured probability of winning (green/red points). We model each mechanism separately (colored bars) by either adding depolarizing noise following the single-qubit (SQ) or two-qubit (2Q) gates, using Cirq [66], or by randomly flipping bits in the simulated bit strings to model readout errors. These error processes are simulated with the measured single-qubit Pauli error  $e_p^{sq}$ , two-qubit Pauli error  $e_p^{2q}$ , and readout error rates  $e_0$  ( $0 \rightarrow 1$ ) and  $e_1$  ( $1 \rightarrow 0$ ) for the qubits involved. We also perform simulations with all error mechanisms enabled simultaneously (black stars), which are consistent with the per-mechanism estimates within uncertainties. Because Variation II directly measures the third Pauli in each context, it requires additional gates and therefore exhibits a higher loss rate. Simulations are performed with 10,000 shots and are therefore subject to statistical uncertainties, which are reflected in the error bars on the black stars. These error bars do not reflect uncertainty due to imprecision in measurements of the physical error rates or due to limitations of the model (e.g. errors may not be exactly depolarizing, and other sources of error such as  $T_1$  decay were not included). Nevertheless, the agreement with the experimental win rate suggests that we have correctly captured the major sources of error.

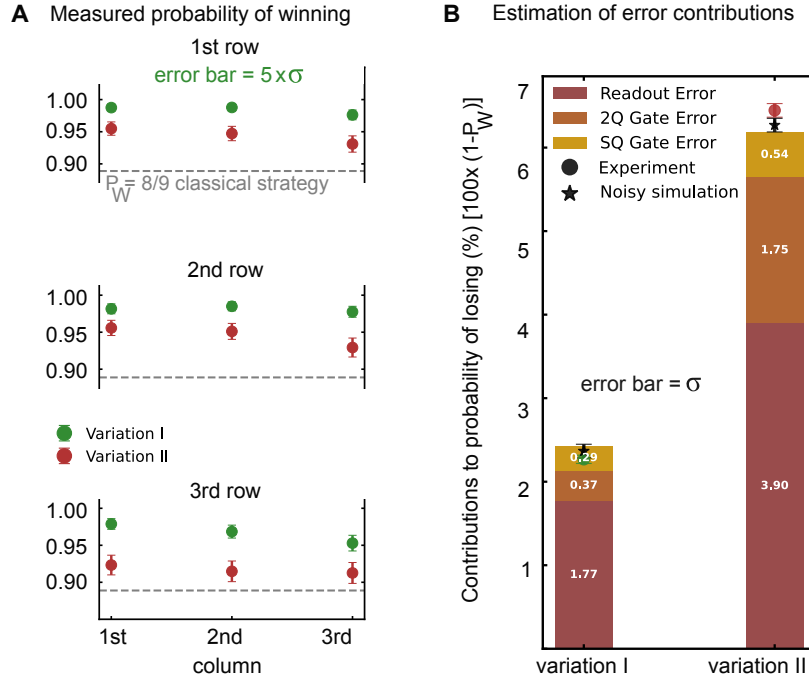


FIG. S3. **Comparing the performance of game variations.** (A) Win probabilities for Variation I (green) and Variation II (red) across the 9 distinct games ordered by the corresponding row-column intersection. The average win probability is  $P_w = 0.9773 \pm 0.0005$  for Variation I and  $P_w = 0.9355 \pm 0.0008$  for Variation II. Each game is played  $N_s = 10,000$  times. The error bars represent five times the standard error. (B) Colored bars represent the simulated contributions of individual error mechanisms to the total probability of losing. Black stars show simulations with all mechanisms enabled. Points (green/red) show the measured average loss probability for each variation. Error bars in this panel indicate the standard error.



## 4. KOCHEN-SPECKER-BELL INEQUALITY: FURTHER DATA AND CALIBRATION

### 4.A. Continuous Measurement of a Random Sequence

To evaluate  $\chi_{\text{KSB}}$ , we stream a random sequence of 180 measurement contexts, rows or columns from the Mermin-Peres square (table I of the main text), and collect statistics over  $N_s = 1000$  runs of such sequences. If a measurement Pauli  $P$  appears in two consecutive compatible contexts, that is, with only commuting operators in between (compatible contexts, e.g.,  $X_2$  in Fig. S4(A), green), the two outcomes, in principle, should agree, so  $P_{\text{agree}} = 1$ . We experimentally measure  $P_{\text{agree}}$  for every Pauli over all such compatible occurrences and plot the results in Fig. S4(A) (right). The binomial standard error is

$$\sigma = \sqrt{\frac{P_{\text{agree}}(1 - P_{\text{agree}})}{N_c}}, \quad (\text{S1})$$

with  $N_c = 20,000$ , the average number of occurrences of each Pauli. If a given Pauli (e.g.,  $X_2$  in Fig. S4(B), red) is measured before and after a context incompatible with it ( $Z_2, Z_1, Z_1Z_2$ ), the two measurement results should be fully uncorrelated. For such instances, the measurements for all Paulis are shown in Fig. S4(B) (right), with uncertainties from Eq. (S1).

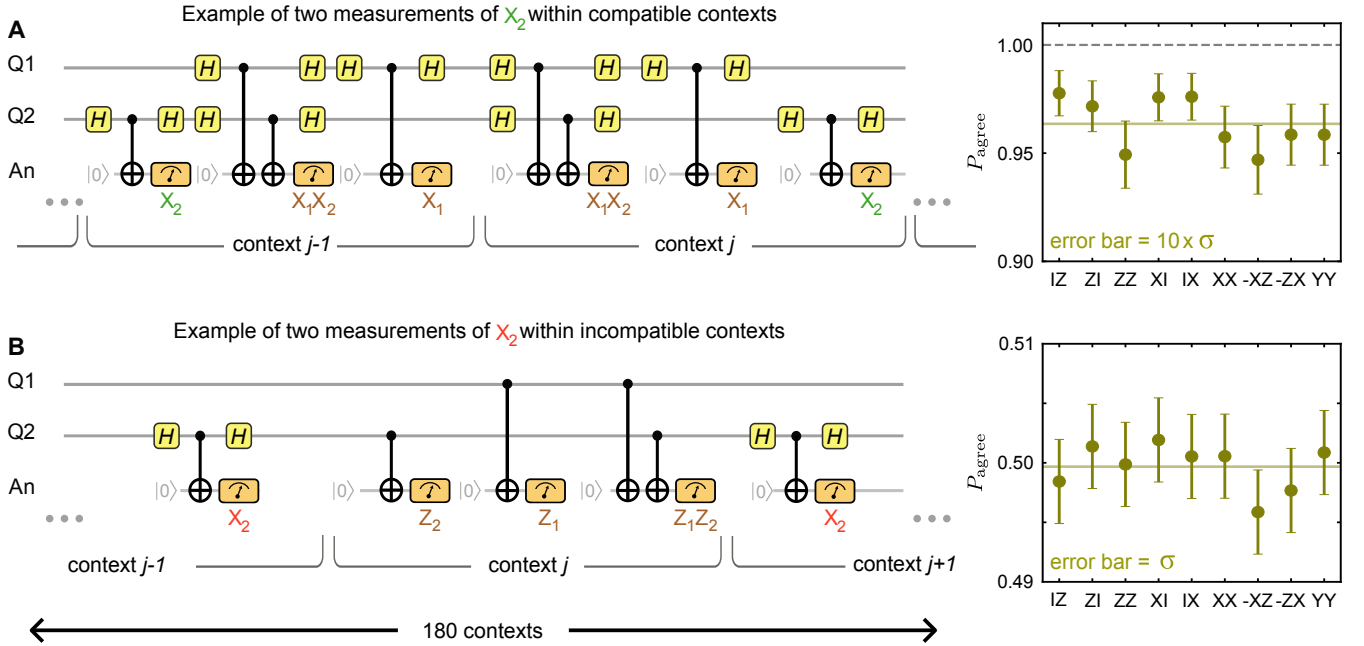


FIG. S4. (A) Example segment where a Pauli (here  $X_2$ ) is measured twice with only commuting operators between contexts  $j-1$  and  $j$ , implying  $P_{\text{agree}} = 1$ . Right:  $P_{\text{agree}}$  for each Pauli over all such compatible occurrences. The horizontal solid line is the average  $P_{\text{agree}} = 0.9636 \pm 0.0004$ . The error bars in the plot are  $10 \times \sigma$  for visibility. (B) Example segment where intermediate operators do not commute with  $X_2$ , implying  $P_{\text{agree}} = 1/2$ . Right:  $P_{\text{agree}}$  for each Pauli over all such incompatible occurrences. The horizontal solid line is the average  $P_{\text{agree}} = 0.500 \pm 0.001$ .

#### 4.B. Calibrating Compensation Phases

To continuously measure the two-qubit Pauli operators that enter  $\chi_{KSB}$ , we map the joint state of Q1 and Q2 onto the phase of an ancilla qubit. Figure S5(A) illustrates the circuit used to implement this mapping. In this construction, the ancilla is highly sensitive to undesired phase accumulation. Between successive two-qubit Pauli measurements, the ancilla is measured and reset, a process that requires large frequency excursions in our architecture. The finite settling time associated with these excursions introduces additional phase accumulation on the qubits, which in turn produces a distribution of  $\chi_{KSB}$  values that depends on the flux-line transfer function of each ancilla qubit.

To compensate for this effect, we insert a virtual Z rotation before the final Hadamard in each two-qubit Pauli mapping sequence (Fig. S5(B)) and calibrate its value to cancel the accumulated phase. Figure S5(C) shows the estimated  $\chi_{KSB}$  as a function of the applied virtual Z.

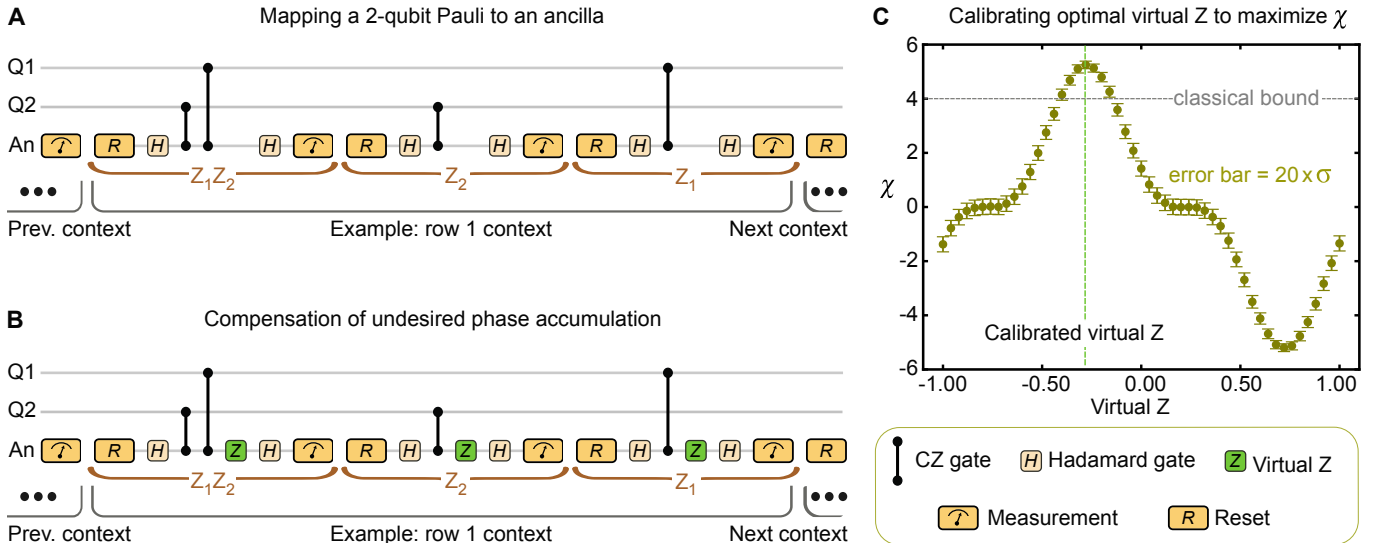


FIG. S5. **Compensating undesired phase accumulation.** (A) Example segment within the 180-context sequence where we measure row 1. (B) To compensate for the undesired phase accumulation, we introduce virtual Z gates before each final Hadamard during a Pauli mapping. (C) Calibrating the optimal virtual Z (applied in (B)) that will maximize the value of  $\chi_{KSB}$ . The error bars plotted are 20 times the statistical uncertainty derived from the binomial distribution.

## 5. GHZ STATE: FIDELITY AND ERROR ESTIMATION

### 5.A. Fidelity

#### a. Definition

We aim to estimate the fidelity of the experimentally prepared state,  $\tilde{\rho}_{\text{GHZ}}$ , with respect to the  $N$ -qubit GHZ state,

$$|\text{GHZ}\rangle = \frac{|0\rangle^{\otimes N} + |1\rangle^{\otimes N}}{\sqrt{2}}. \quad (\text{S2})$$

The fidelity is defined as

$$F \equiv \langle \text{GHZ} | \tilde{\rho}_{\text{GHZ}} | \text{GHZ} \rangle. \quad (\text{S3})$$

Expanding the state  $\tilde{\rho}_{\text{GHZ}}$  in the Pauli basis,

$$\tilde{\rho}_{\text{GHZ}} = \frac{1}{2^N} \mathbb{I} + \sum_{i=1}^{4^N-1} c_i \hat{P}_i, \quad (\text{S4})$$

where  $\hat{P}_i$  are  $N$ -qubit Pauli operators, and the  $c_i$  are the real-valued Pauli expansion coefficients, and substituting this expansion into Eq. (S3) gives

$$F = \frac{1}{2^N} + \sum_{i=1}^{4^N-1} c_i \langle \text{GHZ} | \hat{P}_i | \text{GHZ} \rangle. \quad (\text{S5})$$

Since the GHZ state is a stabilizer state, it has  $2^N$  stabilizer operators  $\{\hat{S}_i\}$ . For these operators

$$\langle \text{GHZ} | \hat{S}_i | \text{GHZ} \rangle = 1, \quad (\text{S6})$$

whereas for all other Pauli operators  $\hat{P}'_i$ ,

$$\langle \text{GHZ} | \hat{P}'_i | \text{GHZ} \rangle = 0. \quad (\text{S7})$$

The fidelity  $F$  can therefore be expressed in terms of the stabilizer coefficients as

$$F = \sum_{i=0}^{2^N-1} c_i, \quad (\text{S8})$$

where the sum is restricted to the  $2^N$  stabilizers. In particular,  $c_0$  is the expansion coefficient of the identity stabilizer,  $c_0 = 1/2^N$ . From Eq. (S4), these coefficients are

$$c_i = \frac{1}{2^N} \text{Tr}[\tilde{\rho}_{\text{GHZ}} \hat{S}_i]. \quad (\text{S9})$$

Thus, the fidelity is the arithmetic mean of the stabilizer expectation values

$$F = \frac{1}{2^N} \sum_{i=0}^{2^N-1} \langle \hat{S}_i \rangle, \quad (\text{S10})$$

where  $\langle \hat{S}_i \rangle$  denotes the expectation value of stabilizer  $\hat{S}_i$  in state  $\tilde{\rho}_{\text{GHZ}}$ . As shown in Refs. [67, 68], this quantity can be estimated by Monte Carlo sampling over a polynomial number of stabilizers, thereby avoiding the exponential cost of full  $N$ -qubit tomography.

*b. Stabilizers*

The  $N$ -qubit GHZ state  $|\text{GHZ}\rangle$  is a stabilizer state with  $2^N$  stabilizers generated by  $N$  independent stabilizers, which can be chosen to be

$$\hat{Q}_i = \begin{cases} \hat{Z}_i \hat{Z}_{i+1}, & i \in \{0, 1, \dots, N-2\}, \\ \prod_{j=0}^{N-1} \hat{X}_j, & i = N-1. \end{cases} \quad (\text{S11})$$

The stabilizers  $\hat{S}_i$  can be written in terms of these generators as

$$\hat{S}_i = \hat{Q}_{N-1}^{i_{N-1}} \hat{Q}_{N-2}^{i_{N-2}} \cdots \hat{Q}_0^{i_0}, \quad (\text{S12})$$

where  $i_k$  denotes the  $k$ th binary digit of  $i$ . The  $2^{N-1}$  stabilizers with  $i_{N-1} = 0$  are *Z-type stabilizers*, diagonal in the computational basis. The remaining  $2^{N-1}$  stabilizers with  $i_{N-1} = 1$  are *X-type stabilizers*, which involve measurements in rotated bases  $X$  and  $Y$ . The total fidelity can be expressed in terms of the average fidelities of these two classes as

$$F = \frac{F^X + F^Z}{2}. \quad (\text{S13})$$

### 5.B. Error Estimation

*a. Fidelity under  $T_1$  with Dynamical Decoupling*

To estimate the fidelity of the GHZ state, we consider a mean relaxation time  $T_1$  for all qubits. Let  $\tau$  denote a small idle interval, the amplitude-damping rate is

$$\gamma \equiv \frac{\tau}{T_1}. \quad (\text{S14})$$

A general single-qubit density matrix, with unit trace and positivity constraints, takes the form

$$\rho = \begin{pmatrix} p_0 & c \\ c^* & p_1 \end{pmatrix}, \quad p_0, p_1 \geq 0, \quad p_0 + p_1 = 1, \quad |c|^2 \leq p_0 p_1. \quad (\text{S15})$$

Here  $p_0$  and  $p_1$  denote the ground- and excited-state populations, respectively, while  $c$  encodes the coherence between the two states. The amplitude-damping channel with Kraus operators

$$K_0 = \begin{pmatrix} 1 & 0 \\ 0 & \sqrt{1-\gamma} \end{pmatrix}, \quad K_1 = \begin{pmatrix} 0 & \sqrt{\gamma} \\ 0 & 0 \end{pmatrix}, \quad (\text{S16})$$

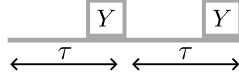
acts on  $\rho$  as

$$\Lambda(\rho) = \sum_i K_i \rho K_i^\dagger = \begin{pmatrix} p_0 + \gamma p_1 & \sqrt{1-\gamma} c \\ \sqrt{1-\gamma} c^* & (1-\gamma) p_1 \end{pmatrix}. \quad (\text{S17})$$

When using dynamical decoupling, this interval is split into two equal halves of duration  $\tau = dt/2$ . Considering a particular dynamical decoupling sequence, the time duration can be separated by a  $Y$  pulse, followed by another  $Y$  (so that the net unitary is identity). For simplicity, we assume the  $Y$  gates are applied instantaneously. The amplitude-damping parameter per half-interval becomes

$$\gamma = \frac{dt}{2T_1}. \quad (\text{S18})$$

After a single cycle of the Amplitude Damping— $Y$ —Amplitude Damping— $Y$  sequence as illustrated below, the density matrix evolves as:



$$\rho \mapsto \rho_{\text{final}}(\tau) = \begin{pmatrix} (1-\gamma)p_0 + \gamma p_1 & (1-\gamma)c \\ (1-\gamma)c^* & \gamma p_0 + (1-\gamma)p_1 \end{pmatrix} + \mathcal{O}(\gamma^2). \quad (\text{S19})$$

Passing to the limit of a large number of dynamical decoupling cycles in time  $t \gg dt$ , the differential equation for the ground-state population is

$$\frac{dp_0}{dt} = \frac{1}{2T_1} (1 - 2p_0), \quad (\text{S20})$$

With the initial condition  $p_0(0)$  at  $t = 0$ , and denoting the ground-state population at time  $t$  as  $p_0(t)$ , the solution to the differential equation is

$$p_0(t) = e^{-t/T_1} (p_0(0) - \frac{1}{2}) + \frac{1}{2}, \quad p_1(t) = e^{-t/T_1} (p_1(0) - \frac{1}{2}) + \frac{1}{2}. \quad (\text{S21})$$

The coherence term decays as

$$c(t) = c(0) e^{-t/(2T_1)}. \quad (\text{S22})$$

Application of the resulting many-cycle channel to the four density matrix components of an  $N$ -qubit GHZ state with idle times  $t_i$  on the  $i^{\text{th}}$  qubit yields:

$$|0\rangle^{\otimes N} \langle 0|^{\otimes N} \mapsto \prod_{i=0}^{N-1} \frac{1}{2} (1 + e^{-t_i/T_1}) |0\rangle^{\otimes N} \langle 0|^{\otimes N} + \prod_{i=0}^{N-1} \frac{1}{2} (1 - e^{-t_i/T_1}) |1\rangle^{\otimes N} \langle 1|^{\otimes N}, \quad (\text{S23})$$

$$|1\rangle^{\otimes N} \langle 1|^{\otimes N} \mapsto \prod_{i=0}^{N-1} \frac{1}{2} (1 - e^{-t_i/T_1}) |0\rangle^{\otimes N} \langle 0|^{\otimes N} + \prod_{i=0}^{N-1} \frac{1}{2} (1 + e^{-t_i/T_1}) |1\rangle^{\otimes N} \langle 1|^{\otimes N}, \quad (\text{S24})$$

$$|0\rangle^{\otimes N} \langle 1|^{\otimes N} \mapsto \prod_{i=0}^{N-1} e^{-t_i/(2T_1)} |0\rangle^{\otimes N} \langle 1|^{\otimes N}, \quad (\text{S25})$$

$$|1\rangle^{\otimes N} \langle 0|^{\otimes N} \mapsto \prod_{i=0}^{N-1} e^{-t_i/(2T_1)} |1\rangle^{\otimes N} \langle 0|^{\otimes N}. \quad (\text{S26})$$

Thus, the transformed density matrix, after discarding terms orthogonal to the GHZ state, is

$$\begin{aligned} \rho_{\text{GHZ}} = \frac{1}{2} \left[ \frac{1}{2^N} \left( \prod_{i=0}^{N-1} (1 + e^{-t_i/T_1}) + \prod_{i=0}^{N-1} (1 - e^{-t_i/T_1}) \right) (|0\rangle^{\otimes N} \langle 0|^{\otimes N} + |1\rangle^{\otimes N} \langle 1|^{\otimes N}) \right. \\ \left. + \prod_{i=0}^{N-1} e^{-t_i/(2T_1)} (|0\rangle^{\otimes N} \langle 1|^{\otimes N} + |1\rangle^{\otimes N} \langle 0|^{\otimes N}) \right]. \quad (\text{S27}) \end{aligned}$$

The resulting fidelity is

$$F_{T_1} = \langle \text{GHZ} | \rho_{\text{GHZ}} | \text{GHZ} \rangle = \frac{1}{2} \left[ \frac{1}{2^N} \prod_{i=0}^{N-1} (1 + e^{-t_i/T_1}) + \frac{1}{2^N} \prod_{i=0}^{N-1} (1 - e^{-t_i/T_1}) + \prod_{i=0}^{N-1} e^{-t_i/(2T_1)} \right]. \quad (\text{S28})$$

The first two terms contribute to the  $Z$ -type fidelity, as they arise from the diagonal elements of the density matrix and are affected only by  $X$ -type Pauli errors. In contrast, the final term originates from the off-diagonal coherence and is therefore sensitive to  $Z$ -type Pauli errors, contributing to the  $X$ -type fidelity.



*b. Fidelity under Single-Qubit Gates*

To estimate the effect of single-qubit gate errors on the GHZ fidelity, we model each gate by a local depolarizing channel with Pauli error rate  $e_p^{\text{sq}}$ . Because any nontrivial Pauli error reduces the fidelity, the contribution from  $n_{\text{sq}}$  number of single-qubit gates is

$$F_{\text{sq}} = (1 - e_p^{\text{sq}})^{n_{\text{sq}}}. \quad (\text{S29})$$

For the  $Z$ -type fidelity, only  $X$  and  $Y$  Pauli errors contribute,

$$F_{\text{sq}}^Z = (1 - \frac{2}{3}e_p^{\text{sq}})^{n_{\text{sq}}}, \quad (\text{S30})$$

and since the total fidelity is defined as the arithmetic mean of the  $X$ - and  $Z$ -type contributions,

$$F_{\text{sq}}^X = 2F_{\text{sq}} - F_{\text{sq}}^Z. \quad (\text{S31})$$

*c. Fidelity under Two-Qubit Gates*

Similarly, let  $n_{2q}$  denote the number of two-qubit gates, each followed by local depolarizing channels on the involved qubits with error rate  $e_p^{2q}$ . Out of the 15 non-identity two-qubit Pauli operators, all but  $ZZ$  reduce the GHZ fidelity. Thus, the effective error probability is  $\frac{14}{15}e_p^{2q}$ , and

$$F_{2q} = (1 - \frac{14}{15}e_p^{2q})^{n_{2q}}. \quad (\text{S32})$$

For the  $Z$ -type fidelity, only  $ZZ$ ,  $IZ$ , and  $ZI$  errors leave the stabilizers unchanged, giving

$$F_{2q}^Z = (1 - \frac{12}{15}e_p^{2q})^{n_{2q}}. \quad (\text{S33})$$

Since the total fidelity is defined as the arithmetic mean of the  $X$ - and  $Z$ -type contributions, we obtain

$$F_{2q}^X = 2F_{2q} - F_{2q}^Z. \quad (\text{S34})$$

*d. Fidelity under Readout Error*

To estimate the fidelity contribution from readout errors, we model the readout channel with Kraus operators

$$k_0 = \begin{pmatrix} \sqrt{1-e_0} & 0 \\ 0 & 0 \end{pmatrix}, \quad k_1 = \begin{pmatrix} 0 & 0 \\ \sqrt{e_0} & 0 \end{pmatrix}, \quad k_2 = \begin{pmatrix} 0 & \sqrt{e_1} \\ 0 & 0 \end{pmatrix}, \quad k_3 = \begin{pmatrix} 0 & 0 \\ 0 & \sqrt{1-e_1} \end{pmatrix}, \quad (\text{S35})$$

where  $e_0$  and  $e_1$  denote the probabilities of misidentifying  $|0\rangle$  and  $|1\rangle$ , respectively. For a qubit in state  $\rho$ , measurement in the  $Z$  basis under this channel yields

$$\sum_i \text{Tr}(k_i \rho k_i^\dagger Z) = \sum_i \text{Tr}(\rho k_i^\dagger Z k_i) \equiv \text{Tr}(\rho Z_\Lambda), \quad (\text{S36})$$

where the transformed observable is

$$Z_\Lambda = (e_1 - e_0) \mathbb{I} + (1 - e_0 - e_1) Z. \quad (\text{S37})$$

By inserting basis changes before the readout channel, the corresponding transformed observables for  $X$  and  $Y$  are

$$X_\Lambda = Y^{1/2} Z_\Lambda Y^{-1/2} = (e_1 - e_0) \mathbb{I} + (1 - e_0 - e_1) X, \quad (\text{S38})$$

$$Y_\Lambda = X^{-1/2} Z_\Lambda X^{1/2} = (e_1 - e_0) \mathbb{I} + (1 - e_0 - e_1) Y. \quad (\text{S39})$$

The expectation value of any stabilizer is obtained by replacing each Pauli operator with its corresponding transformed observable. The resulting fidelity under asymmetric readout error, incorporating the effect on the expectation values of the  $X$ - and  $Z$ -type stabilizers of the GHZ state, is

$$F_{\text{readout,asym}} = \frac{1}{4} \left[ (1 - e_0)^N + e_0^N + (1 - e_1)^N + e_1^N \right] + \frac{1}{2} (1 - e_0 - e_1)^N + \frac{1}{2^{N/2}} (e_1 - e_0)^N \cos\left(\frac{\pi N}{4}\right). \quad (\text{S40})$$

Since in practice  $e_0 \approx e_1 \lesssim 1\%$ , as shown in Fig. S1, it is convenient to approximate the asymmetric model by the symmetric case  $e_0 = e_1 = \varepsilon$ . Under this assumption, the total fidelity simplifies to

$$F_{\text{readout,sym}} = \frac{1}{2} \left[ (1 - 2\varepsilon)^N + (1 - \varepsilon)^N + \varepsilon^N \right]. \quad (\text{S41})$$

The corresponding fidelities for  $X$ -type and  $Z$ -type stabilizers are

$$F_{\text{readout,sym}}^X = (1 - 2\varepsilon)^N, \quad F_{\text{readout,sym}}^Z = (1 - \varepsilon)^N + \varepsilon^N. \quad (\text{S42})$$

Finally, we approximate all error channels as independent. In our framework, the fidelity is estimated post measurement and therefore includes readout errors, consistent with the conditions of the GHZ game. The combined fidelity is bounded by the product of contributions from the independent error channels,

$$F_{\text{total}} = F_{T_1} \times F_{\text{sq}} \times F_{2q} \times F_{\text{readout,sym}}. \quad (\text{S43})$$

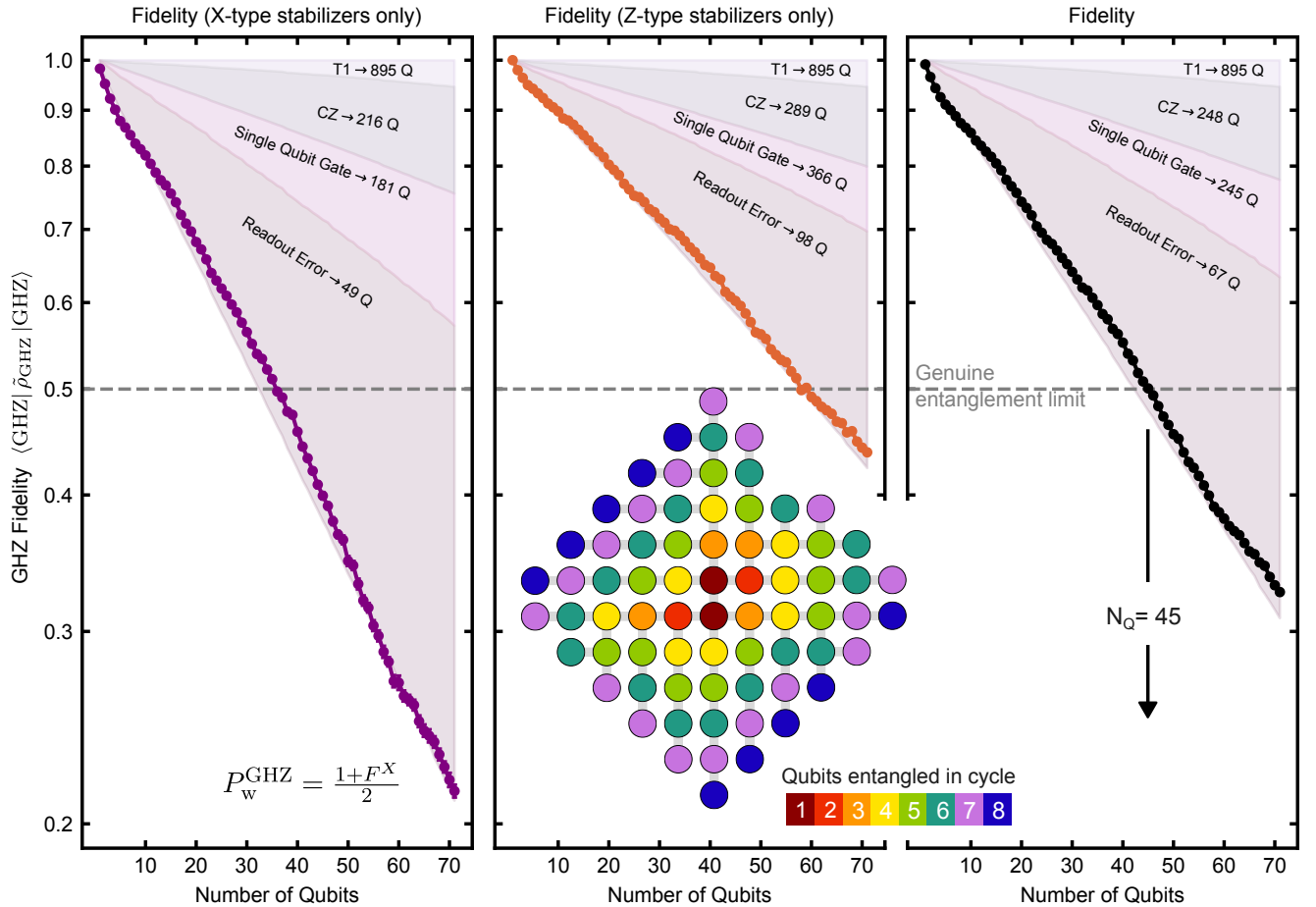


FIG. S6. **Experimental and estimated  $X$ -type,  $Z$ -type, and total fidelities of the GHZ state as a function of system size, up to 71 qubits.** Shaded regions indicate the contributions of individual error channels, with mean values used for all estimates (see Section 5B): single-qubit Pauli error  $e_p^{\text{sq}} = 5 \times 10^{-4}$ , two-qubit Pauli error  $e_p^{2q} = 3 \times 10^{-3}$ , symmetric readout error  $\varepsilon = 7 \times 10^{-3}$ , and relaxation time  $T_1 = 73 \mu\text{s}$ . The measured total fidelity drops below 0.5 at  $N = 45$ , which serves as a witness of genuine  $N$ -partite entanglement (the genuine entanglement limit). Labels within the shaded regions mark the system size at which each channel alone would reduce the fidelity below 0.5. The shaded wedge corresponding to single-qubit errors is relatively large due to the additional single-qubit gates introduced by dynamical decoupling. Inset: representative two-dimensional GHZ growth pattern, with colors denoting the entangling-cycle index at which qubits are added to the GHZ state.

### 5.C. GHZ State Growth and Fidelity

The growth of an  $N$ -qubit GHZ state is implemented using a randomized breadth-first search (BFS) [69] on a two-dimensional qubit grid. The procedure begins with a single qubit and expands outward by sequentially entangling neighboring qubits. At each step, the set of unentangled qubits adjacent to the GHZ state is identified, and the order of their inclusion is randomized by shuffling this set. This stochastic growth path distributes the effect of local noise and device-specific imperfections. Averaging results over multiple randomizations yields spatially homogeneous statistics. The entangling CNOT operation is realized with a gate sequence {Hadamard, CZ, Hadamard} on the target qubit, which incorporates a new qubit into the existing GHZ state. Owing to the radial expansion on a two-dimensional geometry, the required two-qubit gate depth scales approximately as  $\sqrt{N}$ .

For each system size, we generate 50 randomized growth patterns and, for each pattern, perform 20 independent instances of the GHZ game (choices of the  $x_i$ ). This results in  $N_g = 1000$  games per system size, with each game executed  $N_s = 1000$  times. In each shot, a win is recorded when the parity of the measured output bitstring fulfills the GHZ winning condition defined in the main text. The mean winning probability, averaged across the 50 randomizations, is shown in Fig. 3 of the main text. The standard error of the mean is given by

$$\sigma_N = \frac{SD_{50}}{\sqrt{50}}, \quad (\text{S44})$$

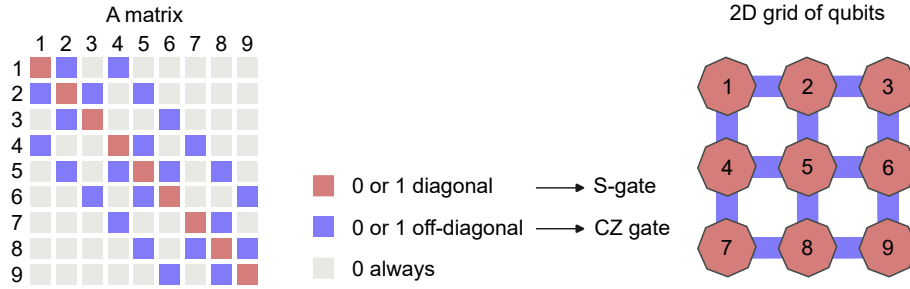
where  $SD_{50}$  denotes the standard deviation of the average win rate across the 50 growth patterns. The winning probability of the GHZ game,  $P_w^{\text{GHZ}}$ , is directly related to the  $X$ -type stabilizer fidelity,  $F^X$ , through  $P_w^{\text{GHZ}} = (1 + F^X)/2$ . The total GHZ fidelity is obtained as the average of the  $X$ - and  $Z$ -type stabilizer fidelities. To obtain both contributions,  $Z$ -type measurements are interleaved with the game experiments, and the order of all circuits is randomized. Error suppression is implemented through dynamical decoupling and randomized compiling (one instance per  $X$ -type stabilizer circuit). Fig. S6 summarizes the measured  $X$ -,  $Z$ -, and total fidelities, together with an error analysis described in Section 5B.

## 6. SHALLOW CIRCUITS AND HIDDEN LINEAR FUNCTION (HLF) PROBLEM

### 6.A. Formalism and Further Experimental Data

Our work experimentally implements the two-dimensional Hidden Linear Function (HLF) problem [3], comparing the two-qubit gate depth required to obtain exact solutions with the corresponding classical circuit depth needed for exact evaluation. We note that the theoretical results of Ref. [3] establish a quantum-classical separation for circuits achieving correctness with probability  $p = 7/8$ , whereas our implementation operates in the regime of exact solutions.

The minimum classical circuit depth required to implement a Boolean function with  $s$  inputs, that depends on each input, using two-input, one-output gates, is  $\log_2(s)$ . To encode the two-dimensional Hidden Linear Function (HLF) problem [3] on a square qubit grid, the diagonal entries of the defining matrix  $A$  are mapped to S gates on individual qubits, while the off-diagonal entries correspond to CZ gates between qubits. Pairs of qubits that are not connected in the two-dimensional geometry always correspond to zero entries in  $A$ . An illustrative example of mapping a  $n \times n$  matrix  $A$ , with  $n = 9$ , onto a grid is shown below.



Because all Boolean inputs of the 2D HLF problem acquire a geometric representation, the total number of inputs can be counted directly from the grid. A lower bound on the number of classical circuit layers to exactly solve the HLF problem is given by

$$L_{\text{classical}} = \log_2(\text{number of edges} + \text{number of nodes}), \quad (\text{S45})$$

where the terms *edges* and *nodes* refer to the elements of the grid's graph. This expression provides a measure of classical computational complexity for comparison with the quantum implementation.

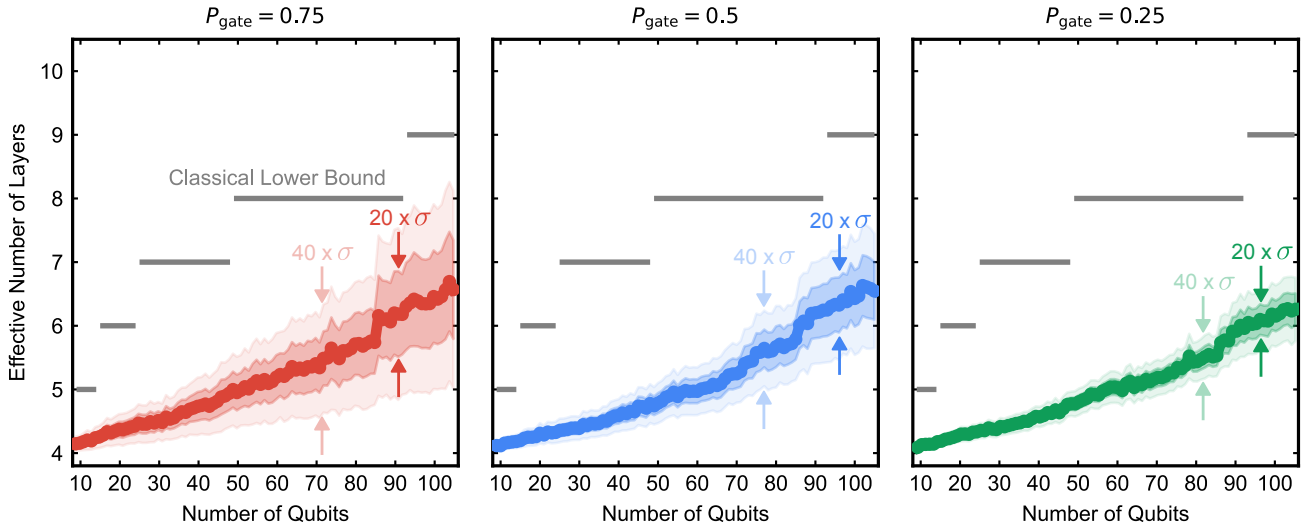


FIG. S7. **Additional data for finding solutions of 2D hidden linear functions experiment at different gate application probabilities.** The trends indicate that a similar number of effective two-qubit layers is required to solve the HLF problem at a given dimension. Shaded regions denote confidence intervals: dark shading corresponds to  $\pm 10\sigma$  and light shading to  $\pm 20\sigma$ . Numerical studies up to a few tens of qubits indicate that an extensive set of bitstrings represents valid solutions for a given problem, so that even in the presence of errors, the measured output bitstring may yield a correct solution.

For the quantum case, the target unitary is implemented using  $S$  gates together with four layers of CZ gates. Fig. 4 shows representative 2D HLF instances, constructed by randomly applying gates to the allowed geometry with probability  $P_{\text{gate}} = 0.5$  and evaluated in terms of the effective number of two-qubit layers (defined in the main text and also in Section 6B). Additional data are provided in Fig. S7, including gate application probabilities of  $P_{\text{gate}} = 0.25$  and  $0.75$  for both  $S$  and CZ gates, complementing the results in Fig. 4. For each system size, the mean value is computed as the average over  $N_g = 1000$  random HLF instances, each executed  $N_s = 100$  times. The standard error of the mean is obtained from the distribution of results across the same ensemble and is defined as

$$\sigma_N = \frac{SD_{1000}}{\sqrt{1000}}, \quad (\text{S46})$$

with  $SD_{1000}$  denoting the standard deviation across the ensemble of 1,000 HLF problems.

### 6.B. Lower Bound Analysis

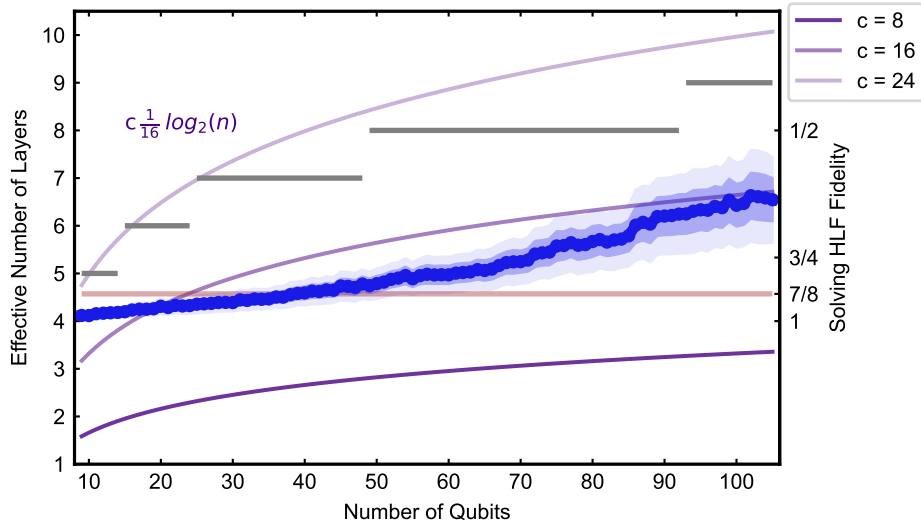


FIG. S8. **Effective number of layers to obtain a solution to the HLF problem as a function of the encoding size.** The experimental data from our implementation (blue) are compared with several candidate classical bounds. The three curves correspond to parameterized lower bounds of the form  $c \log_2(n)/16$ , obtained by extrapolating the asymptotic result of Ref. [3] into the experimentally relevant regime as the scaling parameter  $c$  is varied. The red horizontal line marks the  $7/8$  fidelity.

To enable a practical comparison with the classical lower bound, defined in terms of computational time or circuit depth, we adopt a resource-based figure of merit commonly used for benchmarking noisy quantum systems: the Time-To-Solution (TTS) metric; see Fig. S8. This metric quantifies the total temporal cost required for a quantum processor to reliably solve a problem, thereby incorporating the impact of noise on algorithmic performance. The TTS is defined as the product of the physical circuit depth,  $D_{\text{physical}}$ , and the inverse of the observed success probability,  $P_{\text{success}}$ :

$$\text{Effective Depth (TTS)} = D_{\text{physical}} \times \frac{1}{P_{\text{success}}}. \quad (\text{S47})$$

The quantity  $1/P_{\text{success}}$  represents the number of repetitions required to obtain the correct bitstring with high confidence on a noisy device, and therefore quantifies the associated quantum resource overhead. By converting this probabilistic performance into an “Effective Depth,” the TTS metric enables a direct comparison of quantum resource requirements against the theoretical classical depth lower bound for the HLF problem. We employ this Effective Depth metric to position contextuality-based tasks as a metrological standard for quantum computation, shifting the emphasis from complexity-theoretic supremacy proofs toward rigorous, hardware-level benchmarking.

The argument of Bravyi *et al.* applies in the asymptotic limit of large problem size  $n$  and lies well outside the regime accessible to near-term quantum devices. This limitation can be appreciated through a simple estimate. Consider an HLF instance of size  $n = 65,000$ , corresponding to an  $n \times n$  matrix. Extrapolating the theoretical result of Ref. [3] to this “small” value of  $n$  implies that a classical circuit of depth  $1 \sim \log_2(n)/16$  layers of two-bit, two-fan-in gates



would already succeed with probability at least  $7/8$ . For smaller  $n$ , the asymptotic argument becomes unreliable, and no functional dependence is known for the performance of optimal classical algorithms. Moreover, the theoretical lower bound on circuit depth,  $D$ , pertains to worst-case complexity and does not directly apply to noisy, finite-sized quantum processors. For example, the minimum quantum circuit depth implied by the theory would require an unattainably large device ( $n = 2^{64}$  for  $D = 4$ ), underscoring the gap between asymptotic results and present hardware capabilities. In the absence of a closed-form expression that allows a direct comparison with classical performance, we provide a conjecture in Section 6A. The corresponding classical circuit depth is plotted as gray horizontal lines in Fig. S8.

We further compare our experimental results with the theoretical predictions of Ref. [3]. We first note that the bound derived by Bravyi *et al.* applies to circuits that solve the HLF problem with success probability exceeding  $7/8$ . It is therefore instructive to identify where the performance of our quantum processor falls below this threshold. As shown in Fig. S8, the data intersect the horizontal line at  $4/(7/8)$  (red) at approximately  $N \sim 35$  qubits. Interpreting this crossing through the asymptotic formula would suggest the existence of a depth-1 classical circuit that outperforms our device at this point. However, this conclusion is an artifact of extrapolating an asymptotic bound far outside its valid regime and should not be taken as a meaningful prediction for finite-size experiments.

A second possible comparison is obtained by introducing a prefactor  $c$  into the functional form of the Bravyi *et al.* and examining its consistency with the data at moderate system sizes. Assuming the scaling with  $n$  remains valid while allowing the overall constant to vary, we find in Fig. S8 that for  $c = 8$  the classical curve lies entirely below the data, for  $c = 16$  it intersects the data near  $N \sim 20$ , and for  $c = 24$  the data remain below the curve across the full range shown.